Lithos 296–299 (2018) 563–579

Contents lists available at ScienceDirect

Lithos

journal homepage: www.elsevier.com/locate/lithos

Interaction of mantle magmas and fluids with crustal fluids at the 1894 Ma Montviel alkaline-carbonatite complex, Canada: Insights from metasomatic and hydrothermal carbonates

Olivier Nadeau [a,*], Ross Stevenson [b], Michel Jébrak [b]

[a] University of Ottawa, Ottawa, Ontario, Canada
[b] Université du Québec à Montréal, Montreal, Quebec, Canada

ARTICLE INFO

Article history:
Received 8 June 2017
Accepted 19 November 2017
Available online 27 November 2017

Keywords:
Carbonatites
Alkaline magmas
Mantle fluids
Metasomatism
Nd
Sr
C and O isotopes

ABSTRACT

Alkaline and carbonatite rocks are relatively rare but offer the opportunity to study the contribution of fluids in the genesis of mantle and crustal rocks because they are commonly affected by metasomatism. Carbonate minerals represent versatile archives of mantle and crustal magmatic-hydrothermal processes because they can have magmatic, metasomatic or hydrothermal origins and because they host the trace elements, stable and radiogenic isotopes required to unravel their petrogenesis. Previous studies have shown that the 1894 Ma Montviel alkaline carbonatite complex was emplaced through four injections of volatile-saturated, mantle magmas which evolved through fractional crystallization, mixing of mantle and crustal fluids and metasomatism. Trace element analyses and $\delta^{18}O$, $\delta^{13}C$, $^{87}Sr/^{86}Sr$ and $^{143}Nd/^{144}Nd$ isotope compositions of metasomatic and hydrothermal carbonates further support that each magma injection was accompanied by a volatile phase. Variations in trace element concentrations suggest that the carbonatite might have exsolved from a metasomatized mantle or hybrid silicate carbonatite magma, and that the fluid composition evolved towards higher REE and lower HFSE with increasing degree of segregation of the carbonatite magma and the silicate source. A strong correlation between the C-O-Sr isotopic systems show that mantle fluids mixed with crustal fluids, increasing the $^{87}Sr/^{86}Sr$ from mantle to crustal values, and driving the C and O isotopic ratios towards respectively lighter and heavier values. The Sm/Nd isotopic system was weakly coupled with the other isotopic systems as depleted mantle fluids mixed with crustal fluids and metasomatized the crystallizing magmas, thereby redistributing the REE and affecting their Sm/Nd ratios. The Nd isotopes suggest that the mixed mantle/crustal fluids redistributed the rare earth elements, producing ultra-depleted ($\varepsilon_{Nd} = +10$), normally depleted ($\varepsilon_{Nd} = +4$) and slightly enriched ($\varepsilon_{Nd} = -2$) isotopic compositions.

1. Introduction

Alkaline carbonatite complexes represent ideal natural laboratories to study the interactions that may exist between mantle/crustal magmas and fluids because they are commonly affected by metasomatism – fenitization (e.g., Le Bas, 1987; Pirajno, 2013). Furthermore, carbonate minerals are versatile archives of mantle/crustal magmatic-hydrothermal processes given that: (1) they may originate from magmatic, metasomatic and hydrothermal processes; and (2) they host the trace elements, stable and radiogenic isotopes which can be used to unravel their magmatic-hydrothermal petrogenesis (Kerrich et al., 1987; Hecht et al., 1999; Nadeau et al., 2014). Carbonates are ubiquitous in alkaline carbonatite complexes such as Montviel.

The Montviel alkaline carbonatite complex was first described by Barker (1975), prospected for Nb, P, REE, Th, fluorite, barite, Cu and PGE since 1977, and mapped by the Ministry of Energy and Natural Resources of Quebec (Goutier, 2006) (see 'History' in Nadeau et al., 2015 for a more complete story). Montviel's carbonatite and the associated REE mineralization in the form of REE-bearing carbonates and fluorocarbonates have been described previously based on drill core data and subsurface mapping (Nadeau et al., 2015). Subsequent articles by the same research group documented the magmatic origin of the alkaline carbonatite complex using a combination of petrography, mineral and whole-rock geochemistry and Nd-isotope compositions (Nadeau et al., 2016a, 2016b). These studies have shown that the complex was emplaced through a series of four injections of volatile-saturated, mantle magmas which evolved via fractional crystallization, mixing of mantle and crustal fluids and metasomatism. The aim of the present study is to shed light on the role of mantle and crustal fluids in the petrogenesis of the alkaline complex by using combined isotopic

* Corresponding author.
E-mail address: onadeau@uottawa.ca (O. Nadeau).

https://doi.org/10.1016/j.lithos.2017.11.027
0024-4937/

(C-O-Sr-Nd) and trace element geochemistry of the metasomatic and hydrothermal carbonate minerals hosted in the different lithologies.

2. Material and methods

A total of 47 samples were mounted on polished thin sections, observed and analyzed using a conventional petrographic microscope as well as a Hitachi TM300 Tabletop scanning electron microscope (SEM) equipped with a Bruker Quantax 70 energy dispersive x-ray spectrometer (EDS). Selected carbonates from these polished sections were analyzed for Ca, Mg, Fe, Mn, Sr, and Si using a JEOL JXA-8900 L electron microprobe (EMP) with a 10 to 40 μm diameter, 15 kV and 20 nA beam in the Geochemical Laboratories at McGill University, Montreal, Canada. The instrument was calibrated using a set of commercial standards. Counting time was 20 s for all elements. Relative standard deviations (1σ) were generally <1% (e.g., CaO = 50.0 ± 0.5 wt%) and limits of detection were around 500 ppm.

Incompatible trace elements were analyzed in the same crystals using laser ablation ICPMS at the Geotop laboratories of UQAM, Montreal. Although there is a certain degree of uncertainty that the exact same grains were analyzed in all cases due to the fact that the laser was not pointed directly on the spot that was analyzed by electron microprobe, and may have thus analyzed a crystal of a slightly different composition. The system consists of a Photon-machines Analyte.193 G2 Pulse Excimer laser attached to a Nu Instrument Attom, high resolution, sector field ICPMS. The laser conditions varied between a 20 μm beam using 100% of 3 J/cm^2 at 5 Hz to a 150 μm beam using 33% of 1 J/cm^2 at 20 Hz. The system was monitored using a NBS610 glass standard. Trace element concentrations were quantified using a USGS MACS3 calcite and Ca determined from the electron microprobe. When analyzed as an unknown, the NBS610 glass standard reproduced the official trace element concentrations with <20% relative standard variation.

Radiogenic isotopes were analyzed in the Geotop laboratories at UQAM, Montreal. Carbonate minerals were extracted using a hand drill equipped with a small diamond drill bit and a fraction of this powder was set aside for stable isotope analyses. Sample weighing and chemistry were performed in a class 100 (ISO5) clean room. Powdered samples were weighed (about 0.1 g) and a ^{149}Sm—^{150}Nd spike was added to determine Sm and Nd concentrations. Samples were dissolved in 0.5 M acetic acid on hot plates for 2 h, subsequently centrifuged, and the supernate was pipetted out and dried overnight. Dry samples were dissolved in 3 N HNO_3 and eluted twice through Teflon columns with Sr-specific resin to collect Sr. Samarium and Nd fractions were then purified by cation exchange chromatography following the procedure of Roulleau and Stevenson (2013). The Sr samples were mounted on single Re filaments, the Sm and Nd samples were mounted on double Re filament and all samples were measured in static collection mode on a Thermo Scientific Triton Plus thermal ionization mass spectrometer (TIMS). The Sr and Nd isotope compositions were monitored using the NBS987 Sr and JNd$_i$ standards which returned values of ^{87}Sr/^{86}Sr value of 0.70125 ± 0.00003 (2σ error, n = 27) and ^{143}Nd/^{144}Nd = 0.512096 ± 0.00012 (2σ error, n = 10), respectively, during the analytical period. Typical combined procedure blanks for Nd and Sm were <150 pg.

Stable isotopes were analyzed in the Geotop laboratories at UQAM, Montreal. A polished section of each sample was first analyzed by electron microprobe to identify the carbonate minerals. For calcites about 120 μg, and for other carbonates about 150 to 450 μg of sample was weighed into a glass micro-crucible using a micro-balance. The crucibles were pre-cleaned in 5% nitric acid in a sonic bath for 20 min, rinsed 3 times in de-ionized water and dried overnight in an oven (60 °C). Each weighted sample was transferred in a conical base borosilicate vial capped with a septum. The vials were pre-cleaned using the same technique as that described above for the crucibles. The samples were placed in a heated rack at 90 °C for one hour prior to analysis. Samples were analyzed using a Micromass Isoprime universal triple collector IRMS in Dual Inlet mode coupled to a MultiCarb system in Geotop laboratories, UQAM. For each sample three drops of orthophosphoric acid (ρ = 1.92 g/cm^3) were added under vacuum. The resulting CO_2 was trapped in a cold finger at −180 °C (liquid nitrogen) for 10 min. A water trap (−70 °C) condensed moisture between the vial and the cold finger. The CO_2 was then heated at −60 °C and focused on a second cold finger at −160 °C for 5 min. The resulting gas was finally released in a fixed volume and the pressure of the reference gas was equilibrated with that of the sample. The monitoring gas is a Jackson Dome CO_2 with a δ^{13}C of −3‰ VPDB and a δ^{18}O of 25.8‰ VSMOW. For each analytical sequence reference materials were interspersed with the unkowns for normalization on the VPDB and VSMOW scales. The reference materials used are: (1) 'UQ6' calcite, with δ^{13}C = +2.25‰ VPDB and δ^{18}O = +29.47‰ VSMOW; (2) NBS18 calcite, with δ^{13}C = −5.01 ± 0.03‰ VPDB and δ^{18}O = +7.19 ± 0.23‰ VSMOW; and (3) an 'in-house' Mt. St-Hilaire, gem-quality magnesian-ankerite crystal with δ^{13}C = −5.61 ± 0.07‰ VPDB and δ^{18}O = 18.66 ± 0.19‰ VSMOW.

3. Geology

Alkaline and carbonatite rocks are relatively rare and are usually found in continental rifts, ocean islands and collisional orogens. Orogenic alkaline carbonatite complexes are thought to be emplaced during the late stage of the orogen, during orogenic collapse, extensional tectonics, and possible slab delamination and asthenosphere up flow (Smithies and Champion, 1999; Chiarabba et al., 2014). Although Paleoproterozoic magmatic activity is generally rare within the Superior Province, a number of other alkaline intrusions of similar age to the Montviel Complex do occur such as the 1907 Ma Cargill pyroxenite carbonatite complex (Sage, 1988) and the 1872 Ma Borden silicocarbonatite carbonatite complex (Bell et al., 1987) in the Kapuskasing Subprovince. The origin of Montviel, Cargill and Borden alkaline carbonatite complexes is unclear but may be related to post-orogenic extension occurring on the outskirts of the craton and related readjustments along major fault zones (Condie et al., 2015).

The 1894.2 ± 3.5 Ma (David et al., 2006) Montviel alkaline complex intrudes the Archean foliated Nomans tonalite which is regionally metamorphosed to greenschist facies (Fig. 1). Extensive diamond drilling, field and drill core cross-cutting relationships, and surface and subsurface mapping established a relative chronological sequence for the petrologic evolution of the Montviel alkaline carbonatite complex (Corta and Berthelot, 2002; Goutier, 2006; Mulja, 2006; Desharnais and Duplessis, 2011; Nadeau et al., 2015, 2016a, 2016b). The sequence began with the emplacement of the alkaline carbonatite complex through a series of four magma injections (Nadeau et al., 2016a, 2016b). The first pulse of mantle magmatism produced the clinopyroxenites, melano- to leucosyenites and a suite of melteigites-ijolites. Field and cross-cutting relationships led Goutier (2006) to suggest that this first pulse was followed by the intrusion of a riebeckite-granite, most probably through partial melting of crustal rocks, which is in agreement with its ε_{Nd} value of −2.3 (Nadeau et al., 2016b). A second pulse of magmatism resulted in silicocarbonatites (10–50% modal carbonates), displaying 'lamprophyric' and 'kimberlitic' resemblances, which are crosscut by-, and intermingled with calciocarbonatites and ferrocarbonatites. These carbonatites were subsequently cut by a third pulse of magmatism consisting of relatively late, dyklets, pods and lenses of intermingled silico-, calcio- and ferrocarbonatites. These two injections of silicocarbonatites and carbonatites intruded the center of the alkaline complex and their fluids apparently did not affect the previously emplaced silica-undersaturated rocks. These three pulses were finally cut by a 50 m.-wide dyke of silicocarbonatite of 'kimberlitic' resemblance and a polygenic, diatreme breccia, both of which also do not seem to have metasomatized the previously injected rocks. Although not metamorphosed, the complex is intensely altered, showing pervasive as well as channelized and selective Na-metasomatism (e.g., aegirine-augite and aegirine, albite, analcime), K-metasomatism (e.g., biotite, microcline), Fe-metasomatism (e.g., Fe-

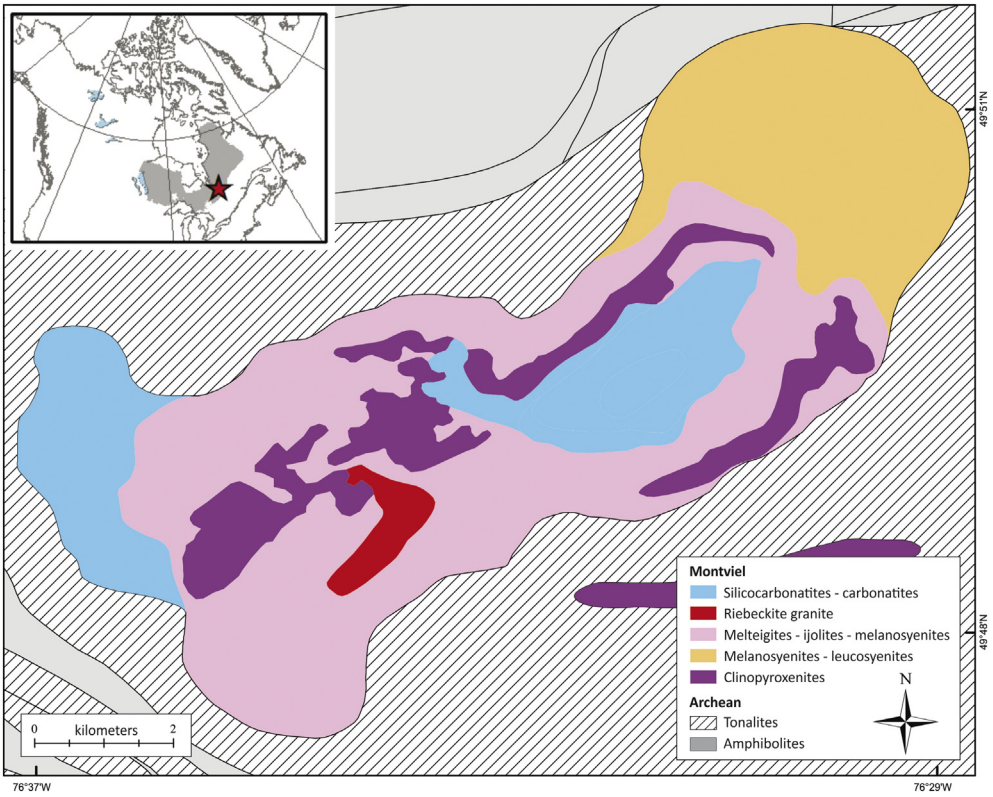

Fig. 1. Geological map of Montviel alkaline carbonatite complex. Modified after Goutier (2006) and Nadeau et al. (2016a).

dolomite, ankerite, siderite), Ba-, Sr-, F- and P-metasomatism (e.g., barytocalcite, strontianite, fluorite, fluorapatite, Ba-Sr-bearing calcite, dolomite and ankerite, REE-Ba-Sr bearing (fluoro)carbonates, barite, monazite and xenotime) (Nadeau et al., 2016a, 2016b). The identified REE-bearing carbonates and fluorocarbonates include burbankite-(Ce), carbocernaite-(Ce), ewaldite-(Y), huanghoite-(Nd), cordylite-(Ce), cordylite-(Nd), kukharenkoite-(Ce), qaqarssukite-(Ce) and synchysite-(Ce) (Nadeau et al., 2015).

3.1. Clinopyroxenites

In the field and in drill cores, clinopyroxenites, melteigites, ijolites and melanosyenites are observed as dykes, pods, sills and lenses that cross-cut each other. For example, clinopyroxenite commonly hosts pods of ijolite and melanosyenite whereas ijolites and melanosyenites commonly host pods of clinopyroxenite. The clinopyroxenite does not look like a cumulate, and consist of coarse augite and aegirine-augite, titanite and biotite with pyrrhotite, chalcopyrite, sphalerite and ilmenite (Figs. 2a, 3a-b). Augite is systematically metasomatized to aegirine-augite, sometimes to aegirine, and also to biotite, along fractures and grain boundaries. Feldspathoids are represented by nepheline, sodalite, analcime (a zeolite) and cancrinite (a pseudo-zeolite), which all display secondary alteration or recrystallization textures. Accessory minerals include fluorapatite and zircon. Calcite, dolomite and ankerite sometime show textures that are unequivocally hydrothermal or metasomatic such as veinlets and their selvages, respectively. Unfortunately, it is not possible to assign a magmatic origin to carbonates based solely on petrographic relations.

3.2. Melteigites and Ijolites

The melteigites and ijolites are found in association with clinopyroxenites and melanosyenites and are always metasomatized. Melteigites consist of coarse augite altered to aegirine-augite and aegirine, along with significant amounts of coarse biotite, titanite and fluorapatite (Figs. 2b, 3c-d). Abundant microscopic nepheline, sodalite, cancrinite and analcime appear to be secondary. The ijolites are very similar to melteigites but contain less clinopyroxene and more nepheline and analcime (Fig. 2c).

3.3. Syenites and granites

The syenites are commonly associated with melteigites-ijolites and clinopyroxenites and range in composition from K-feldspar clinopyroxenites to quartz leucosyenites. They resemble ijolites but contain greater amounts of microcline and albite and less nepheline, cancrinite and analcime. The melanosyenites consist of ferropotassic magnesio-hastingsite, riebeckite, aegirine-augite and microcline. Aegirine-augite and albite are secondary. The leucosyenites (Fig. 2d) are the only quartz-saturated rocks of the alkaline complex, along with the riebeckite granite described below, and occur only in the NE end of the alkaline complex (Fig. 1). The riebeckite granite outcrops only in the southern part of the intrusion and was mapped as a single unit (Goutier, 2006; Nadeau et al., 2015). The granite resembles the leucosyenite but contain significantly more quartz and plagioclase, and relatively less microcline (Fig. 3e-f). Biotite and riebeckite are present in minor amounts. Hydrothermal alteration has altered plagioclase to albite and produced riebeckite from an unidentified ferromagnesian mineral.

3.4. Silicocarbonatites

Silicocarbonatites at Montviel have compositions intermediate between ultramafic undersaturated silicate rocks (clinopyroxenites, melteigites, ijolites and melanosyenites) and carbonatites, and contain 10–50% carbonate minerals. Silicocarbonatites are subdivided into

glimmerite breccias, lamprophyric- and kimberlitic silicocarbonatites: The terms 'lamprophyric' and 'kimberlitic' are introduced to enable distinction of the two types of silicocarbonatites and because the silicocarbonatites have visual similarity with ultramafic lamprophyres and kimberlites. Lamprophyric silicocarbonatites are most common and consist of kinked or folded booklets of biotite and pseudomorphs

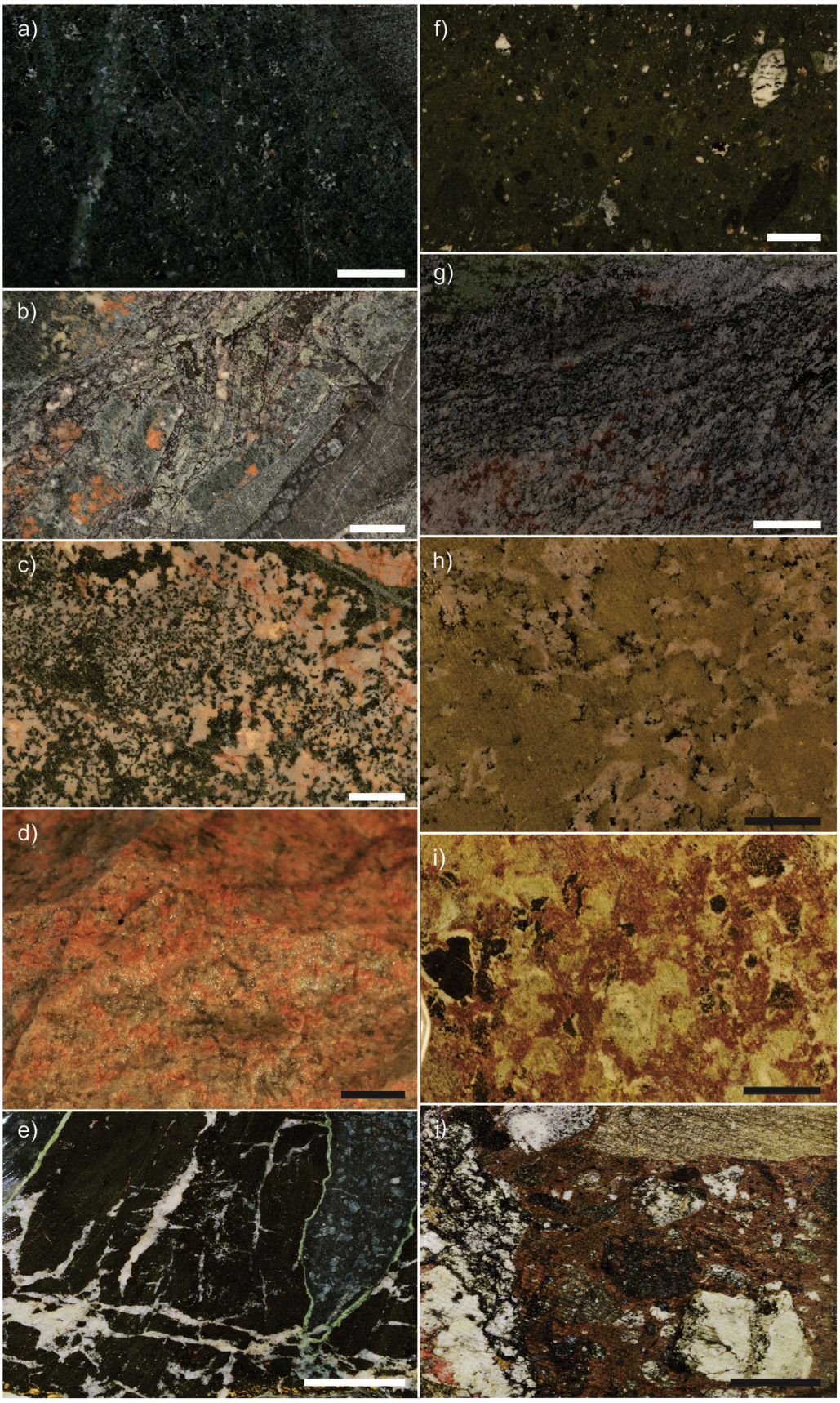

of olivine in a matrix of dolomite, ankerite, calcite and pyrite. Glimmerite breccias consist of decussate-textured glimmerites brecciated by what looks like dyklets of diverse carbonates (Fig. 2e). Kimberlitic silicocarbonatites are found chiefly as a 50 m. wide dyke cross-cutting through all silicate rocks and carbonatites, and consist of a breccia made of altered fragments and xenocrysts of carbonatites and ultramafic-mafic rocks, in a hydrothermally-altered matrix of biotite, aegirine-augite, magnesia-hornblende, albite, calcite, Fe-dolomite, fluorapatite, titanite, zircon, pyrite, chlorite, ilmenite, fluorite and undifferentiated REE-bearing fluorocarbonates (Fig. 2f). They texturally and visually resemble kimberlites but with higher amounts of carbonates, lesser amounts of K-bearing minerals and no fresh olivine.

3.5. Carbonatites

Calciocarbonatites are dominated by calcite and range from barren, unaltered calcite carbonatite to REE-bearing, hydrothermally altered calciocarbonatites. They contain major amounts of what looks like primary calcite and dolomite which are cut by veinlets of ankerite, strontianite, witherite and barytocalcite. They also contain minor to trace concentrations of aegirine-augite, biotite, fluorapatite, barite and REE carbonates and fluorocarbonates (Fig. 2g). Ferrocarbonatites are the most abundant type of carbonatites and seem to replace the calciocarbonatites, suggesting that they might have originated from metasomatism of the calciocarbonatite. They are always strongly and pervasively hydrothermally altered. They are dominated by hydrothermal or metasomatic ankerite and Fe-dolomite, siderite, barytocalcite, strontianite, witherite, fluorite, fluorapatite and minor to trace amounts of biotite, aegirine, arfvedsonite, barite, REE carbonate and fluorocarbonate, monazite-(Ce), xenotime-(Y), sphalerite and galena (Figs. 2h-I, 3g-j). The hydrothermally altered ferrocarbonatites are cross-cut by a series of metric- to sub-metric injections of intermingled silicocarbonatites, calciocarbonatites and ferrocarbonatites, gathered under the term of 'mixed carbonatites'. These mixed carbonatites were also hydrothermally altered to various degrees with alteration products similar to those described above, but interestingly bring into contact altered ferrocarbonatites cut by fresher calciocarbonatites, suggesting that carbonatites were injected repeatedly and episodes of alteration of calciocarbonatites to ferrocarbonatites were followed by episodes of mixed carbonatite magmatism. This leads to the idea that each injection of magma was accompanied by its own fluids, and is discussed further below.

3.6. Polygenic breccia

The polygenic breccia consists of clasts and xenocrysts of silicocarbonatites, carbonatites and ultramafic-mafic rocks in a pervasively altered matrix of dolomite, calcite, ankerite, strontianite, barytocalcite, fluorapatite, biotite, aegirine-augite, and ferropotassic magnesio-hastingsite (Fig. 2j). Three-dimensional modeling of the breccia suggests that the shapes are a hybrid between dykes and a diatreme (Nadeau et al., 2013), and Nadeau et al. (2015) proposed that the breccia unit formed as a result of high-energy fragmentation with significant displacement based on modeling of the distribution and size of the fragments (Jebrak, 1997) and three dimensional modeling of the deposit based on drill core data. This explosion was the last event of the emplacement of the Montviel alkaline complex.

3.7. Mineral Paragenesis

A mineral paragenesis was established based on relative chronology and petrological observation of the field and drill cores (Nadeau et al., 2016a). Olivine was only observed in three of the lithologies: as pseudomorphs in clinopyroxenites and kimberlitic silicocarbonatites and as a minor unaltered occurrence in the polygenic breccia. Augite is only found in clinopyroxenites and melteigites whereas aegirine-augite is the most common clinopyroxene in all ultramafic and mafic-, silica-deficient rocks. Aegirine was observed in ferrocarbonatites. Alkaline amphiboles such as ferropotassic magnesio-hastingsite, riebeckite and arfvedsonite were identified in melanosyenites, ferrocarbonatites and kimberlitic silicocarbonatites, respectively. It is noteworthy that biotite and fluorapatite were present throughout the evolution of the complex. Nepheline, sodalite, cancrinite and analcime were observed in clinopyroxenites, melteigites and ijolites. Cancrinite was also seen in lamprophyric silicocarbonatites. Microcline and plagioclase were identified in melanosyenites and leucosyenites whereas quartz was found only in leucosyenites and granites. In the silicate rocks, feldspathoids were found to occur in the early units (melanosyenite, melteigite, ijolite), microcline and plagioclase crystallized in the intermediate units (melano- to leucosyenites) and quartz crystallized in the last silicate rocks (leucosyenite and granite). Metasomatic (alteration) and/or hydrothermal (infills) albite was observed in all silicate rocks. Cutting through these silicate rocks, the silicocarbonatites and carbonatites host no tectosilicates except for albite in some silicocarbonatites samples. Apart from a few veinlets of ankerite, calcite and dolomite were the only carbonates to crystallize in the primitive *Si*-undersaturated rocks. It is not possible to affirm with certitude that all calcite had a magmatic origin but according to extensive petrographic observations, all strontianite, siderite, barytocalcite and witherite are either metasomatic (alteration) or hydrothermal (infills) and were identified exclusively in silicocarbonatites and carbonatites. Dolomite (ferroan) (Fe-dolomite), like calcite, may have had magmatic as well as metasomatic/hydrothermal origins. Primary sulfides consisted on pyrrhotite, chalcopyrite, sphalerite and galena. Most pyrite is secondary and appears to have resulted from low temperature recrystallization, except for some primary pyrite which formed during the last stages of the petrogenesis. Primary oxides consist largely of ilmenite, with some magnetite.

Fig. 2. Macroscopic photographs of lithologies from Montviel. The mineralogy was derived from hand sample descriptions, optical microscopy, scanning electron microscopy with energy dispersive spectrometry, x-ray diffraction and electron microprobe analyses in the wavelength dispersive mode. All scale bars are 1 mm. a) Clinopyroxenite consisting mainly of augite, aegirine-augite, biotite, nepheline, sodalite, cancrinite, carbonates and sulfides. The alteration is pervasive as well as localized through channel flows (sample MV12-UM04). b) Brecciated analcime melteigite consisting mostly of aegirine-augite, aegirine, analcime, biotite, fluoro-magnesio-arfvedsonite, carbonates, fluorapatite and sulfides. Most, if not all minerals are metasomatic and the alteration is pervasive as well as channelized (sample MV12·SY01A). c) Ijolite made of aegirine-augite, biotite, analcime, nepheline, microcline, oxides, carbonates and sulfides. Although the alteration seems subtle, all major phases including aegirine-augite, biotite, analcime and microcline are metasomatic (sample MV12SY02). d) Leucosyenite consisting mainly of microcline, variably albitized plagioclase and quartz. The sample is pervasively and intensely altered (sample MV12-SY04). e) Glimmerite consisting of metasomatic and/or hydrothermal biotite and variably altered pyrochlore, brecciated by dyklets/veinlets of carbonates. The glimmerite is metasomatic and may result from the alteration of an ultramafic precursor, here shown as an enclave circumscribed by greenish veinlets (sample LP12-SICB02A). f) Kimberlitic silicocarbonatite showing angular clasts of mafic-ultramafic and carbonatite lithologies in a metasomatized matrix made of aegirine-augite, biotite, magnesio-hornblende, albite, carbonates and fluorapatite (sample MV12-KI01). g) Calciocarbonatite mostly made of calcite, Fe-dolomite, Mg-ankerite, biotite, aegirine-augite and sulfides. The calcite may or not be magmatic but all Fe-dolomite, Mg-ankerite, aegirine-augite and REE-bearing fluorocarbonates are either metasomatic (alteration) or hydrothermal (infills) (sample MV12·HREE02B). h) Siderite ferrocarbonatite consisting of coarse hydrothermal/metasomatic siderite overprinting Fe-dolomite and calcite, along with biotite, sulfides and undifferentiated REE-bearing fluorocarbonates. Calcite may or not have been magmatic, but siderite appears to be replacing calcite and Fe-dolomite, and is thus interpreted to be metasomatic (sample MV12·CAFECB03). i) Intensely and pervasively altered ferrocarbonatite consisting of Fe-dolomite, Mg-ankerite, siderite, strontianite, witherite, barytocalcite, calcite, fluorapatite, undifferentiated REE-bearing fluorocarbonates, biotite and partly digested clasts of glimmerite and silicocarbonatite (sample MV12-CAFECB01A). j) Diatreme breccia made of clasts of different types of carbonatites and mafic/ultramafic lithologies in a matrix of biotite, fluorapatite, and carbonates (sample MV12.MBX02B).

The cumulate nature of clinopyroxenites implies that fractional crystallization played a role in the evolution of the silicate magma. Furthermore, the continuum in the crystallization of augite and aegirine-augite throughout clinopyroxenite, melteigite, ijolite, melanosyenite and leucosyenite sequence, and the gradual decrease in cpx-to-nepheline ratio from clinopyroxenite through

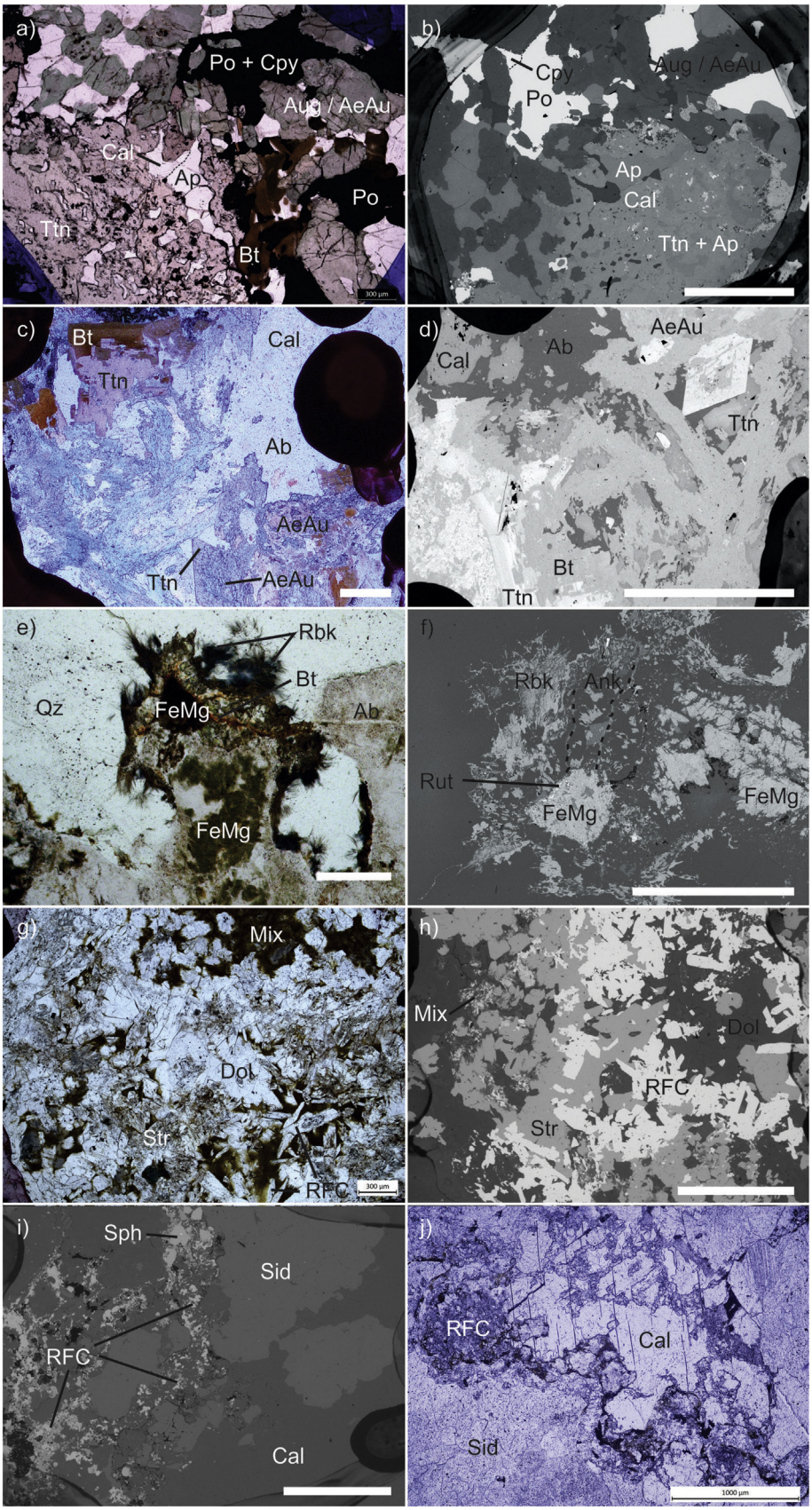

melteigite, ijolite and urtite also points towards fractional crystallization.

4. Results

4.1. Trace element concentrations

Carbonate minerals were identified based on their major element compositions and consisted of calcite, dolomite and Fe-dolomite, ankerite, siderite, strontianite, barytocalcite, along with minor amounts of witherite, magnesite and Ba-Ca-Mg carbonate (Ca-bearing norsethite?) (Table 1). In terms of trace elements, most of these carbonates have Ti ranging from 0.022 to 40 ppm but one analytical point stands out with a concentration of 185 ppm Ti. This point also returned relatively high values of Nb (2.1 ppm), Hf (0.22 ppm) and Ta (0.04 ppm) suggesting that it might contain a HFSE-bearing mineral inclusion (titanite?). The carbonates also have Zr ranging from 0.0005 to 5 ppm although 5 data points returned values of Zr ranging from 7 to 30 ppm and these 5 points are also the most enriched in Hf (0.2 to 0.7 ppm) and relatively enriched in Ta (0.008 to 0.04 ppm), in turn suggesting that some of the HFSE-bearing inclusions also contained Zr (zircon?). Taken as a proxy for REE, most carbonates have Ce concentrations ranging from 0.035 to 11.5 ppm but 7 data points returned Ce ranging from 22 to 66 ppm and these points are also generally enriched in all REE. Given that REE are compatible in carbonates it is possible that the REE are hosted in some of the carbonate's crystal lattices, but it is also possible that some carbonate hosted REE-bearing fluoro carbonate (RFC) mineral inclusions. The concentration of REE in carbonates must have been controlled by the concentration of REE in the fluids but must also have been affected by the presence (or not) of RFC, monazite and xenotime. Given that the REE-bearing phases were heterogeneously distributed among the different lithologies (clinopyroxenites and melteigites contained very little RFC, ijolite, syenite and granite contained no RFC and most RFC, monazite and xenotime were hosted in silicocarbonatites and carbonatites), a certain amount of scatter is expected in the chondrite-normalized REE plots. Furthermore, variations in laser beam sizes and ablation times resulted in variations in limits of detection which also contributed to the heterogeneous aspect of the MORB-normalized spidergram.

Calcite, ankerite, strontianite, barytocalcite, siderite and Fe-dolomite show highly variable chondrite-normalized REE patterns (Fig. 4). The calcites contain REE profiles ranging from about 0.1 times- to over 100 times chondrite LREE, and from below 0.1 times- to below 10 times chondrite HREE. The REE profiles in calcite have negative to flat slopes, with some calcite showing concave down patterns. Only calcites with the strongest LREE enrichments display a negative Ce anomaly. Ankerite display similar ranges in chondrite-normalized REE values, but most ankerite crystals display flat REE patterns, and many show positive, HREE-enriched slopes. Strontianite and barytocalcite display strongly negative slopes and are thus systematically enriched in LREE and depleted in HREE, although the latter has at least one order more HREE than the former. Siderite has a strikingly different REE pattern that is depleted in LREE, enriched in MREE and moderately enriched in HREE, creating a 'Z-type' pattern. Only one Fe-dolomite crystal was analyzed, and it yielded a flat profile that is overall strongly REE depleted. In general, REE concentrations do not appear to be controlled by mineralogy and carbonates do not appear to be buffered with respect to rare earth elements.

The chondrite-normalized REE profiles for carbonates are plotted for the different lithologies present at Montviel (Fig. 5). Carbonates from the clinopyroxenites are relatively LREE-enriched with the degree of enrichment gradually decreasing through the clinopyroxenite-melteigite-ijolite sequence. The granite has carbonates with slightly positive slopes and REE contents less than that of chondrites. The silicocarbonatite contains carbonates that are slightly enriched in REE and strongly enriched in LREE, and are somewhat similar to the enrichments observed in the clinopyroxenite. Calciocarbonatites host carbonates with low REE contents and negative- to positive slopes, but ferrocarbonatites show strong enrichments in REE, and zones enriched in medium to heavy REE. Carbonates from late mixed carbonatites are also enriched in MREE and display the same concave down pattern observed in some of the carbonates from HREE-rich ferrocarbonatite. Finally the polygenic breccia host carbonates strongly enriched in all REE, and strongly enriched in MREE to HREE relatively to other lithologies.

The concentration of large ion lithophile elements (LILE; Sr, Ba), high field strength elements (HFSE; Th, Ta, Nb, Ce, Zr, Hf, Sm, Ti, Y and Yb) were normalized to MORB (McDonough and Sun, 1995) and plotted as spidergrams (Fig. 6). The spidergrams display a variety of patterns which range between two end members. The first end member is characterized by strong positive Yb, Y, Sm, Ce and Th anomalies, and strong negative Ti, Zr, Hf, Nb and Ta anomalies, resulting in a characteristic 'saw-tooth' pattern (e.g., Fig. 6a,b,g,h,j). This 'saw-tooth' pattern is best observed in carbonates from clinopyroxenite and ferrocarbonatite. The other end member displays a 'resorbed saw-tooth' pattern, showing gradually milder positive REE and negative HFSE anomalies (e.g., Fig. 6c,d,e,f). A transition from the 'saw-tooth' to the 'resorbed-saw-tooth' pattern is observed through the clinopyroxenite-melteigite-ijolite sequence, after which the subsequent silicocarbonatites and carbonatites return to the 'saw-tooth' pattern. Finally, the polygenic breccias appear to have a moderately resorbed saw-tooth pattern.

4.2. Isotopic ratios

The carbonates from Montviel have $^{147}Sm/^{144}Nd$ ratios that vary from 0.05 to 0.14 and $^{143}Nd/^{144}Nd$ ratios that vary from 0.511170 to 0.512055 and yield initial ε_{Nd} values ranging from −2 to +10. In Fig. 7a, the carbonates are plotted on a $^{147}Sm/^{144}Nd$ versus $^{143}Nd/^{144}Nd$ diagram along with a reference isochron. The depleted mantle (DM) isochron was arbitrarily fitted using the U—Pb zircon 1894 Ma age of the alkaline complex (David et al., 2006) with a depleted mantle $^{143}Nd/^{144}Nd_{initial}$ of 0.510376. The initial ε_{Nd} value of the chondritic uniform reservoir (CHUR) was calculated based on an present day $^{143}Nd/^{144}Nd$ ratio of 0.512638 and $^{147}Sm/^{144}Nd$ ratios of 0.1966 (Allègre, 2008). The depleted mantle (DM) ε_{Nd} was calculated following Bennett and De Paolo (1987). The diagram shows that the Montviel carbonates do not form an isochron. The lack of coherence in this diagram likely reflects open-system behavior among the different carbonate samples due to hydrothermal alteration and/or crustal fluid assimilation. This open system behavior is evident in Fig. 7b that plots the ε_{Nd} values of the units versus their $^{147}Sm/^{144}Nd$ ratios. In this diagram, the different lithologies form a trend of decreasing ε_{Nd} values and increasing $^{147}Sm/^{144}Nd$ ratios.

Fig. 3. Transmitted light photomicrographs (plane polarized light; PPL) and backscattered electron images (BSE) of selected lithologies from Montviel's alkaline complex showing intense metasomatism and textural relationship among minerals, including carbonates. PPL (a) and BSE (b) views of metasomatized clinopyroxenite showing variably fenitized augite (AeAu), pyrrhotite and chalcopyrite, titanite, calcite and apatite. The scale bar is 1 mm in b (Sample MV12·UM01). PPL (c) and BSE (d) views of metasomatized melteigite showing calcite and biotite as well as metasomatic aegirine-augite, titanite and albite. Scale bars are 400 μm in c and 1 mm in d (Sample MV12·IJ01). PPL (e) and BSE (f) views of a zone of alteration within riebeckite granite. A partly altered-, unidentified ferromagnesian mineral is altered to rutile, biotite and fibrous blue riebeckite. Note the presence of quartz-ankerite veinlets. Both scale bars are 300 μm (sample MV12.GR01). PPL (g) and BSE (h) views of metasomatic dolomitic ferrocarbonatite showing the association of Fe-dolomite with strontianite, REE-bearing fluorocarbonates (RFC) and altered zones of mixed chloritized biotite, strontianite and fluorocarbonates (Mix). The scale bar is 1 mm in h (Sample LP12-CAFECB01A). BSE (i) and PPL (j) views of metasomatic siderite ferrocarbonatite showing the hydrothermal replacement of calcite to siderite and REE-bearing fluorocarbonates. The scale bar is 1 mm in i (Sample MV12·CAFECB02). Abbreviations are as follows: aegirine-augite AeAu, albite Ab, ankerite Ank, apatite Ap, biotite Bt, calcite Cal, chalcopyrite Cpy, dolomite (ferroan) Dol, pyrrhotite Po, REE-bearing fluorocarbonates RFC, riebeckite Rbk, rutile Rut, siderite Sid, strontianite Str, titanite Ttn and unidentified ferromagnesian mineral FeMg.

Table 1
Major, minor and trace element compositions of carbonates from different lithologies from Montviel. CO_2 was calculated to obtain 100% electron microprobe totals.

Lithology	Mineral	Sample	CaO	MgO	FeO	MnO	SrO	$Si0_2$	$C0_2$	Total	Ti	1δ	Sr	1δ	Y	1δ	Zr	1δ	Nb	1δ	Ba	1δ	La	1δ	Ce	1δ	Pr	1δ	Nd
Clinopyroxenite	Cal	MV12·IJ02.C3·P1	54.8	0.11	0.16	0.07	0.71	0.00	44.2	100.0	0.09	0.04	287	16	1.76	0.05	0.03	0.01	0.0007	0.0003	6.1	0.1	8.0	0.2	11.8	0.3	1.30	0.04	5.0
Clinopyroxenite	Cal	MV12·IJ02.C3·P2	54.2	0.05	0.10	0.10	1.2	0.00	44.4	100.0			32	4	1.72	0.05	0.0007	0.0004	0.00009	0.00007	10.7	1.2	6.4	0.2	11.5	0.4	1.34	0.04	5.1
Clinopyroxenite	Cal	MV12·UM01.C1·P1NEW	54.6				0.76	0.20	44.4	100.0	1.4	0.4	555	83	10.4	1.4	1.6	0.4	0.011	0.002	0.41	0.05	28	4	24	3	14	2	49
Melteigite	Cal	MV12·SY01A.C2·P1	50.0	1.24	1.4	0.30	0.30	2.4	44.4	100.0	1.1	0.2	577	83	1.5	0.1			0.022	0.013	8.2	0.5	1.2	0.5	2.3	0.9	0.3	0.1	1.2
Melteigite	Cal	MV12·SY01A.C2·P2	52.3	0.47	0.47		0.65	1.5	44.6	100.0	4.7	1.2	820	110	13	1.6	2.9	1.3	0.07	0.02	5.1	1.2	19	2	35	5	6.5	0.8	30
Ijolite	Cal	MV12·SY02B·C1·P1	54.8	0.07		0.13	0.33	0.60	44.0	100.0	44	2	710	110	0.72	0.08	30	1	0.17	0.03	38.1	2.4	1.3	0.1	2.1	0.1	0.29	0.03	1.2
Ijolite	Cal	MV12·SY02B·C2·P4	55.1			0.32	0.22	0.12	44.1	100.0	1.8	0.7	1720	160	0.25	0.02	1.9	0.8	0.014	0.004	3.0	0.6	0.21	0.02	0.5	0.1	0.070	0.009	0.31
Ijolite	Cal	MV12·SY02B·C4.P3	53.1	0.13	0.40	0.07	1.0	0.46	44.8	100.0	31	6	365	76	0.41	0.07	22	3	0.16	0.05	30.8	5.3	0.9	0.2	1.9	0.4	0.23	0.05	0.9
Ijolite	Cal	MV12·SY02B·C6.P1	54.9			0.29	0.18	0.06	44.6	100.0	0.2	0.1	892	74	0.18	0.01	0.13	0.07	0.0014	0.0009	0.9	0.1	0.043	0.006	0.12	0.01	0.023	0.002	0.13
Granite	Ank	MV12.GR01.C1	27.5	4.28	25.1	0.97	0.08	0.46	41.6	100.0	3.8	1.5	1371	94	1.3	0.1	4.1	0.8	0.017	0.005	4.7	1.7	0.15	0.04	0.34	0.08	0.05	0.01	0.24
Granite	Ank	MV12.GR01.C1	27.3	6.81	21.1	1.13	0.14	1.5	42.0	100.0	20	5	1440	130	1.6	0.2	0.5	0.4	0.54	0.15	1.2	0.8	0.03	0.02	0.08	0.04	0.011	0.004	0.08
Glimmerite breccia	Ank	LP12·UMBX01.C1·P1	28.7	12.67	12.5	1.39	0.26	0.00	44.5	100.0	0.05	0.02	1049	89	0.12	0.01	0.009	0.004	0.011	0.006	2.6	0.5	0.08	0.03	0.12	0.04	0.018	0.006	0.08
Glimmerite breccia	Str	LP12·UMBX01.C1·P2	5.5	0.54	0.59		57.7	0.00	35.7	100.0	1.1	0.5			0.07	0.01	0.7	0.3	0.007	0.001	63	11	2.5	0.2	4.2	0.4	0.45	0.04	1.4
Glimmerite breccia	Ank	LP12·UMBX01.C2·P3	27.5	11.44	13.3	1.42	0.34	2.3	43.6	100.0	6.2	2.4	1720	260	0.41	0.03	4	2	0.12	0.02	6.4	2.2	0.39	0.07	0.7	0.1	0.11	0.02	0.48
Glimmerite breccia	Ank	LP12·UMBX01.C2·P4	27.2	11.12	13.7	1.69	0.23	2.3	43.8	100.0	5.2	2.8	1250	100	0.19	0.02	2.2	1.6	0.08	0.02	5.3	2.0	0.29	0.07	0.6	0.2	0.08	0.02	0.34
Glimmerite breccia	Cal	LP12·UMBX01.C3·P5									185	53	1000	290	0.4	0.1	8.5	2.9	2.1	0.6	28.2	4.9	1.2	0.2	2.2	0.5	0.31	0.06	1.4
Glimmerite breccia	Cal	LP12·UMBX01.C4·P1	52.9	0.18	0.44	0.47	0.38	0.69	44.9	100.0	1.6	0.7	819	86	0.22	0.01	1.1	0.5	0.017	0.004	4.0	0.9	0.19	0.04	0.34	0.07	0.05	0.01	0.18
Glimmerite breccia	Cal	MV12·UMBX01.C1·P4	54.1	0.16	0.50	0.13	0.28	0.85	44.0	100.0	2.6	0.3	1643	93	0.26	0.02	1.6	0.2	0.016	0.003	5.1	0.5	0.7	0.1	1.5	0.2	0.23	0.03	1.0
Glimmerite breccia	Cal	LP12·SICB01·C1.P1	53.7	0.35	0.76	0.24	0.17	0.70	44.1	100.0	1.8	0.8	1100	170	0.10	0.01	1.0	0.6	0.34	0.09	4	1	0.23	0.07	0.4	0.1	0.05	0.01	0.19
Glimmerite breccia	Cal	LP12·SICB01·C4·P1	54.4	0.13	0.32	0.09		0.52	44.5	100.0	12.4	0.9	985	87	0.85	0.07	0.7	0.3	0.25	0.03	226	30	48	10	38	8	19	4	78
Glimmerite breccia	Cal	LP12·SICB01·C5.P1	53.1	0.60	0.67	0.21		1.5	43.8	100.0	9.1	1.7	391	33	0.15	0.03	4.1	1.1	0.08	0.01	11.9	2.5	0.34	0.08	0.7	0.1	0.08	0.02	0.35
Lamprophyric silicocarbonatite	Fe-Dol	MV12·HREE01.C3·P1	27.8	16.1	9.0	0.34		0.65	46.0	100.0	2.9	0.4	1019	72	0.28	0.02	0.13	0.03	0.015	0.005	0.45	0.06	0.062	0.007	0.22	0.02	0.040	0.005	0.19
Calciocarbonatite	Cal	MV12·SICACB02·C1.P1	53.9	0.07	0.41	0.55	0.30	0.00	44.8	100.0	0.3	0.1	630	60	2.1	0.2	0.005	0.003	0.016	0.007	4.6	0.3	0.08	0.02	0.2	0.1	0.05	0.01	0.22
Calciocarbonatite	Cal	MV12·SICACB02·C3.P1	54.2	0.06	0.21	0.61	0.20	0.00	44.8	100.0	0.07	0.04	496	16	0.74	0.03			0.00081	0.00077	1.6	0.2	0.11	0.08	0.3	0.2	0.05	0.02	0.21
Calciocarbonatite	Ank	LP12·CACB01A.C2·P3	28.7	9.0	15.9	1.35	0.12	1.6	43.4	100.0	6.6	2.5	269	27	0.13	0.03	3.5	1.3	0.045	0.012	9.6	2.9	0.25	0.08	0.5	0.1	0.07	0.02	0.23
Ferrocarbonatite (LREE)	Sid	MV12·CAFECB02·C1.P4	0.19	3.8	55.3	2.37		0.04	38.3	100.0	11.7	7.8	56	17	7.4	0.9	1.0	0.6							0.2	0.1			
Ferrocarbonatite (LREE)	Sid	MV12·CAFECB02·C1.P5	0.12	4.4	54.5	2.77		0.00	38.2	100.0	8.4	8.0	58	18	16.8	1.4	1.1	0.8	0.19	0.18	10.5	5.3	0.3	0.1	0.5	0.1			0.6
Ferrocarbonatite (LREE)	Ank	MV12·CAFECB02·C1.P6	29.7	10.3	14.2	2.27	0.07	0.00	43.4	100.0	0.48	0.06	350	32	4.4	0.2	0.005	0.001	0.026	0.003	39	6	19	2	22	1	5.8	0.3	30
Ferrocarbonatite (LREE)	Ank	MV12·FECB02·C1.P1	28.0	8.4	18.0	2.74	0.05	0.12	42.8	100.0	2.7	0.2	564	53	4.4	0.4	0.09	0.01	0.16	0.09	4.6	0.4	0.18	0.03	0.50	0.06	0.08	0.01	0.42
Ferrocarbonatite (LREE)	Str	MV12·FECB02·C1·P2	3.4		0.10		61.5	0.00	35.0	100.0	1.6	0.3			0.14	0.01	0.018	0.002	0.08	0.01	100	19	2.0	0.1	5.1	0.4	0.69	0.04	2.5
Ferrocarbonatite (LREE)	Ank	MV12·FECB02·C3.P1	28.3	13.8	11.1	1.85	0.06	0.00	44.8	100.0	0.56	0.04	531	28	2.2	0.1	0.0005	0.0004	0.0012	0.0004	1.8	0.3	0.037	0.005	0.13	0.01	0.025	0.003	0.13
Ferrocarbonatite (LREE)	Str	MV12·FECB02·C3.P2	3.8		0.40		59.9	0.00	35.8	100.0	0.15	0.01			0.31	0.01	0.027	0.002	0.28	0.03	287	23	0.04	0.02			7.5	0.4	33
Ferrocarbonatite (LREE)	Ank	MV12·FECB02·C4.P1	28.9	13.0	12.0	1.72	0.07	0.03	44.3	100.0	17.4	1.1	437	15	3.4	0.1	0.0025	0.0009	0.10	0.01	2.1	0.2	0.34	0.06	1.1	0.2	0.15	0.02	0.7
Ferrocarbonatite (LREE)	Ank	MV12·FECB02·C4.P2	28.4	10.2	15.2	3.00		0.00	43.1	100.0	0.31	0.07	205	14	0.31	0.03	0.0030	0.0017	0.005	0.001	0.24	0.04	0.011	0.004	0.035	0.006	0.007	0.002	0.037
Ferrocarbonatite (LREE)	Ank	MV12·FECB02·C4.P3	28.3	9.6	15.5	3.24		0.00	43.4	100.0	0.03	0.02	370	57	0.26	0.03	0.005	0.004	0.0029	0.0026	0.7	0.3	0.08	0.04	0.2	0.1	0.03	0.01	0.11
Ferrocarbonatite (HREE)	Cal	MV12.LATE2.C1.P1	53.3	0.28	1.1	0.32	0.28	0.16	44.6	100.0	0.022	0.020	2230	78	26.4	1.2	0.0015	0.0008	0.0030	0.0006	21.9	3.4	0.99	0.04	2.8	0.2	0.55	0.03	3.8
Ferrocarbonatite (HREE)	Cal	MV12.LATE2.C1.P2	53.3	0.13	0.77	0.52	0.52	0.06	44.8	100.0			830	290	3.1	0.2	0.0055	0.0046	0.00019	0.00017	23.2	2.4	1.2	0.2	3.4	0.5	0.7	0.1	4.6
Ferrocarbonatite (HREE)	Str	MV12.LATE2.C1·P3	3.6	0.07			61.2	0.00	35.1	100.0	0.9	0.4			0.11	0.02	0.7	0.3	0.004	0.001	52	8	2.7	0.6	6.0	0.8	0.93	0.05	5.7
Ferrocarbonatite (HREE)	Cal	MV12.LATE2.C2·P2	53.3	0.13	0.67	0.48	0.45	0.32	44.6	100.0	17.1	4.9	4700	1300	8.3	2.3	12.2	3.5	0.05	0.02	79	11	3.3	0.8	8.0	1.9	1.6	0.4	9.0
Ferrocarbonatite (HREE)	Sid	MV12.LATE2.C2·P3	0.13	4.45	53.8	2.58		0.01	39.0	100.0			2820	330	15.3	2.6			0.28	0.24	424	51	1.0	0.5	3.7	0.8	1.0	0.3	6.2
Ferrocarbonatite (HREE)	Ba-Cc	MV12.LATE2.C2·P4	20.6	0.13	0.27		0.26	1.1		100.0	15	3	10,420	340	8.2	0.4	0.8	0.7	1.0	0.3		1500	37.4	1.6	66	3	10.1	0.5	50
Mixed carbonatites	Cal	MV12.LATE3.C2·P1	52.9	0.18	2.0	0.28	0.30	0.08	44.3	100.0			564	42	11.1	0.8			0.005	0.002	12.1	0.8	1.0	0.1	1.9	0.1	0.34	0.02	2.1
Mixed carbonatites	Ba-Cc	MV12.LATE3.C4.P1	21.5				0.08	0.29			4.3	2.3	557	66	4.3	0.6	3.5	1.8	0.019	0.008		2900	1.6	0.2	1.4	0.1	0.20	0.03	1.0
Polygenic breccia	Ank	MV12·HREE03.C2.P4	28.5	7.4	17.5	2.82	0.09	0.54	43.2	100.0	23.4	2.8	1460	180	30	4	7.1	1.0	6.5	1.9	8.7	1.2	7.2	0.6	22	2	3.7	0.5	18
Polygenic breccia	Ank	MV12·HREE03.C2·P5	28.5	12.0	11.4	1.84		0.67	45.6	100.0	6.9	1.3	1100	180	40	6	4.2	1.5	17.6	5.1	33.7	2.9	11.1	1.2	30	4	6.9	0.8	32

Table 1 (*continued*)

Lithology	1δ	Sm	Sm/Nd	1δ	Eu	1δ	Gd	1δ	Tb	1δ	Dy	1δ	Ho	1δ	Er	1δ	Tm	1δ	Yb	1δ	Lu	1δ	Hf	1δ	Ta	1δ	Th	1δ
Clinopyroxenite	0.2	0.79	0.16	0.03	0.142	0.005	0.69	0.03	0.080	0.004	0.38	0.02	0.070	0.004	0.163	0.008	0.018	0.002	0.11	0.01	0.014	0.001					0.0093	0.0007
Clinopyroxenite	0.2	0.75	0.15	0.02	0.193	0.006	0.62	0.03	0.074	0.004	0.35	0.01	0.066	0.003	0.160	0.008	0.018	0.001	0.097	0.006	0.013	0.001					0.0023	0.0004
Clinopyroxenite	6	7.8	0.16	0.9	2.3	0.3	6.5	0.8	0.70	0.09	2.9	0.3	0.49	0.06	1.0	0.1	0.09	0.01	0.41	0.05	0.039	0.005	0.035	0.009	0.0010	0.0004	6.0	0.7
Melteigite	0.3	0.21	0.17	0.03	0.067	0.008	0.22	0.02	0.038	0.003	0.24	0.02	0.051	0.004	0.152	0.009	0.023	0.002	0.18	0.01	0.032	0.003			0.0016	0.0009	0.05	0.02
Melteigite	4	7.3	0.25	1.0	2.0	0.3	6.7	0.9	0.8	0.1	3.8	0.5	0.58	0.08	1.3	0.2	0.12	0.02	0.63	0.08	0.076	0.008	0.07	0.03	0.011	0.004	2.2	0.3
Ijolite	0.1	0.2	0.19	0.1	0.07	0.02			0.013	0.007	0.10	0.04	0.010	0.007	0.09	0.05			0.10	0.06	0.009	0.005	0.7	0.1	0.014	0.008	0.34	0.02
Ijolite	0.04	0.08	0.26	0.01	0.023	0.004	0.08	0.02	0.010	0.002	0.051	0.009	0.012	0.003	0.030	0.007	0.004	0.001	0.021	0.005	0.0025	0.0009	0.04	0.02	0.0013	0.0007	0.02	0.01
Ijolite	0.2	0.13	0.15	0.03	0.023	0.007	0.21	0.07	0.010	0.003	0.06	0.02	0.011	0.005	0.04	0.02	0.003	0.002	0.06	0.03	0.013	0.006	0.6	0.1	0.012	0.007	0.26	0.05
Ijolite	0.01	0.05	0.39	0.01	0.019	0.002	0.060	0.008	0.008	0.001	0.039	0.005	0.008	0.001	0.018	0.003	0.0023	0.0004	0.017	0.003	0.0021	0.0005	0.005	0.003			0.003	0.001
Granite	0.03	0.10	0.42	0.02	0.026	0.005	0.13	0.04	0.022	0.004	0.18	0.03	0.049	0.006	0.16	0.02	0.025	0.004	0.19	0.02	0.031	0.005	0.15	0.02	0.0014	0.0009	0.25	0.05
Granite	0.02	0.04	0.49	0.01	0.019	0.005	0.08	0.02	0.027	0.004	0.22	0.03	0.062	0.007	0.22	0.03	0.033	0.005	0.26	0.03	0.040	0.006	0.007	0.006	0.010	0.003	0.04	0.01
Glimmerite breccia	0.03	0.017	0.21	0.006	0.004	0.002	0.019	0.007	0.004	0.002	0.020	0.005	0.005	0.001	0.014	0.004	0.0018	0.0006	0.016	0.004	0.004	0.002			0.002	0.001	0.009	0.004
Glimmerite breccia	0.1	0.09	0.07	0.01	0.013	0.002	0.039	0.009	0.0019	0.0005	0.006	0.002	0.0007	0.0003	0.003	0.002	0.0005	0.0002	0.003	0.001	0.0003	0.0002	0.014	0.007	0.0009	0.0003	0.020	0.004
Glimmerite breccia	0.09	0.09	0.18	0.02	0.025	0.004	0.12	0.04	0.013	0.003	0.09	0.01	0.016	0.003	0.04	0.01	0.008	0.002	0.06	0.01	0.008	0.002	0.09	0.04	0.011	0.005	0.08	0.02
Glimmerite breccia	0.08	0.06	0.16	0.02	0.010	0.005	0.05	0.03	0.006	0.002	0.033	0.009	0.005	0.002	0.015	0.006	0.003	0.001	0.03	0.01	0.004	0.002	0.06	0.04	0.011	0.004	0.08	0.03
Glimmerite breccia	0.3	0.25	0.18	0.08	0.05	0.02			0.016	0.008	0.08	0.03	0.008	0.003	0.02	0.01	0.006	0.004	0.06	0.02	0.007	0.003	0.22	0.08	0.04	0.02	0.24	0.05
Glimmerite breccia	0.03	0.03	0.18	0.01	0.007	0.002	0.014	0.009	0.0048	0.0009	0.037	0.005	0.010	0.001	0.036	0.005	0.008	0.001	0.075	0.006	0.012	0.001	0.02	0.01	0.0019	0.0007	0.025	0.008
Glimmerite breccia	0.2	0.16	0.15	0.02	0.046	0.007	0.15	0.02	0.017	0.002	0.065	0.007	0.011	0.002	0.023	0.005	0.0021	0.0006	0.017	0.004	0.0013	0.0006	0.04	0.01	0.0005	0.0004	0.15	0.02
Glimmerite breccia	0.05	0.03	0.16	0.01	0.007	0.002	0.02	0.01	0.0035	0.0009	0.03	0.01	0.0045	0.0009	0.009	0.004	0.0020	0.0008	0.014	0.004	0.004	0.001	0.03	0.01	0.005	0.003	0.04	0.01
Glimmerite breccia	16	6.3	0.08	1.2	0.9	0.1	2.0	0.3	0.12	0.02	0.34	0.04	0.040	0.004	0.076	0.009	0.0050	0.0008	0.027	0.004	0.003	0.001	0.012	0.006	0.0010	0.0004	11.6	2.3
Glimmerite breccia	0.08	0.08	0.22	0.02	0.013	0.004	0.07	0.02	0.007	0.002	0.023	0.008	0.005	0.002	0.019	0.006	0.004	0.001	0.019	0.006	0.003	0.001	0.10	0.03	0.002	0.001	0.06	0.01
Lamprophyric silicocarbonatite	0.02	0.07	0.35	0.01	0.027	0.005	0.09	0.03	0.008	0.002	0.05	0.01	0.011	0.002	0.034	0.004	0.004	0.002	0.05	0.01	0.010	0.002			0.005	0.002	0.0025	0.0008
Calciocarbonatite	0.03	0.13	0.58	0.02	0.054	0.006	0.23	0.04	0.048	0.007	0.35	0.05	0.08	0.01	0.26	0.03	0.040	0.003	0.33	0.04	0.044	0.003					0.027	0.006
Calciocarbonatite	0.08	0.09	0.41	0.01	0.031	0.002	0.11	0.01	0.019	0.002	0.12	0.01	0.029	0.003	0.089	0.007	0.012	0.001	0.058	0.006	0.007	0.001					0.004	0.003
Calciocarbonatite	0.07	0.05	0.21	0.02	0.012	0.003	0.04	0.02	0.006	0.002	0.020	0.006	0.005	0.002	0.011	0.004	0.0017	0.0008	0.004	0.003	0.002	0.001	0.09	0.03	0.003	0.002	0.06	0.02
Ferrocarbonatite (LREE)					0.8	0.4			0.3	0.2	1.2	0.7	0.18	0.14	1.3	0.6	0.2	0.1	2.6	1.1	0.6	0.3			0.00000043	0.00000003	0.14	0.06
Ferrocarbonatite (LREE)	0.5				0.4	0.3			0.3	0.2	2.1	0.7	0.64	0.31	3.6	0.8	0.5	0.2	3.2	1.3	0.6	0.3					0.19	0.06
Ferrocarbonatite (LREE)	2	8.2	0.27	0.9	2.1	0.1	5.1	0.2	0.52	0.02	1.7	0.2	0.18	0.02	0.27	0.03	0.022	0.003	0.12	0.01	0.013	0.003					1.8	0.2
Ferrocarbonatite (LREE)	0.06	0.19	0.44	0.03	0.06	0.01	0.26	0.03	0.06	0.01	0.53	0.04	0.14	0.02	0.64	0.08	0.12	0.01	1.08	0.08	0.16	0.02			0.0013	0.0008	0.0038	0.0005
Ferrocarbonatite (LREE)	0.2	0.23	0.09	0.017	0.046	0.004	0.11	0.01	0.006	0.001	0.019	0.003	0.003	0.001	0.006	0.001	0.0006	0.0002	0.003	0.001	0.0003	0.0002					0.009	0.002
Ferrocarbonatite (LREE)	0.01	0.08	0.56	0.01	0.027	0.004	0.15	0.02	0.031	0.003	0.26	0.02	0.074	0.005	0.29	0.02	0.063	0.005	0.59	0.04	0.097	0.006					0.0016	0.0003
Ferrocarbonatite (LREE)	2	3.4	0.10	0.2	0.49	0.03	1.00	0.06	0.049	0.003	0.106	0.007	0.0100	0.0006	0.019	0.002	0.0016	0.0002	0.008	0.001	0.0009	0.0002	0.0012	0.0005	0.00013	0.00007	4.0	0.3
Ferrocarbonatite (LREE)	0.1	0.31	0.42	0.03	0.12	0.01	0.47	0.03	0.105	0.007	0.62	0.03	0.119	0.008	0.28	0.01	0.034	0.003	0.19	0.02	0.020	0.002					0.04	0.02
Ferrocarbonatite (LREE)	0.009	0.022	0.59	0.009	0.005	0.003	0.05	0.05	0.005	0.002	0.04	0.01	0.008	0.002	0.029	0.008	0.005	0.002	0.041	0.009	0.008	0.003						
Ferrocarbonatite (LREE)	0.05	0.04	0.32	0.01	0.010	0.003	0.07	0.01	0.008	0.002	0.043	0.007	0.008	0.001	0.026	0.003	0.0032	0.0009	0.032	0.007	0.004	0.001						
Ferrocarbonatite (HREE)	0.3	3.0	0.79	0.1	1.4	0.2	5.6	0.3	1.21	0.05	7.8	0.3	1.43	0.06	3.1	0.2	0.28	0.02	1.24	0.05	0.110	0.006			0.0003	0.0002	0.140	0.005
Ferrocarbonatite (HREE)	0.6	3.1	0.68	0.3	1.1	0.1	3.4	0.3	0.31	0.02	1.1	0.1	0.14	0.01	0.25	0.01	0.020	0.001	0.100	0.009	0.010	0.001					0.12	0.01
Ferrocarbonatite (HREE)	1.3	2.0	0.35	0.4	0.4	0.1	0.6	0.1	0.018	0.002	0.033	0.007	0.0030	0.0006	0.007	0.002	0.0004	0.0002	0.002	0.001	0.0004	0.0002	0.02	0.01	0.0006	0.0003	0.023	0.004
Ferrocarbonatite (HREE)	2.5	4.9	0.54	1.7	1.6	0.5	4.5	1.6	0.5	0.2	2.6	0.8	0.32	0.1	0.7	0.2	0.04	0.02	0.16	0.06	0.04	0.02	0.20	0.08	0.008	0.006	0.31	0.04
Ferrocarbonatite (HREE)	1.6	11.2	1.81	2.3	3.0	0.9	15	5	1.4	0.5	6.1	2.7	0.84	0.36	1.0	0.5			1.0	0.6							0.8	0.2
Ferrocarbonatite (HREE)	4	18.0	0.36	0.9	5.1	0.5	11.6	1.6	0.8	0.1	2.1	0.3	0.25	0.06	0.51	0.09	0.04	0.02	0.14	0.07	0.003	0.007	0.06	0.04			2.3	0.3
Mixed carbonatites	0.1	1.35	0.64	0.08	0.67	0.05	3.1	0.2	0.62	0.04	3.2	0.2	0.50	0.04	0.91	0.08	0.067	0.006	0.27	0.02	0.026	0.003					0.23	0.05
Mixed carbonatites	0.1	0.8	0.80	0.1	0.50	0.07	1.6	0.2	0.21	0.03	0.8	0.1	0.12	0.01	0.22	0.04	0.02	0.01	0.18	0.03	0.027	0.006	0.10	0.05	0.0021	0.0018	0.9	0.3
Polygenic breccia	2	6.5	0.37	0.8	2.0	0.2	6.8	0.8	1.1	0.1	6.6	0.7	1.2	0.2	3.0	0.4	0.31	0.04	1.5	0.2	0.17	0.02	0.27	0.05	0.008	0.004	34	5
Polygenic breccia	3	12.3	0.39	1.8	3.8	0.6	10.8	1.5	1.6	0.2	9.1	1.4	1.6	0.3	3.7	0.5	0.35	0.05	1.6	0.2	0.18	0.03	0.12	0.03	0.007	0.002	45	5

Table 2
Sm—Nd, Sr, C and O isotope ratios for carbonates from the different lithologies at Montviel.

Lithology	Sample	Mineral	Nd	Sm	$^{147}Sm/^{144}Nd$	$^{143}Nd/^{144}Nd$	2σ error	$^{143}Nd/^{144}Nd_0$	$\varepsilon_{Nd}(t)$	$^{87}Sr/^{86}Sr$	2σ error	$\delta^{13}C$	$\delta^{18}O$
Clinopyroxenite	MV12·IJ02	Carb								0.70186	0.00001	−5.5	10.6
Clinopyroxenite	MV12·IJ02	BC	11.6	1.7	0.08789	0.511455	0.000032	0.510360	3.40	0.71190	0.00002		
Melteigite	MV12·IJ01	BC	8.4	1.6	0.11497	0.511651	0.000024		0.62	0.70392	0.00000	−2.4	11.1
Ijolite	MV12·SY02B	Cal								0.70432	0.00002	−3.6	10.7
Ijolite	MV12·SY02B	BC	21.0	2.5	0.07319	0.511482	0.000007	0.510615	7.51	0.70646	0.00003	−3.6	10.7
Granite	MV12.GR02	BC	1171	210	0.10848	0.511582	0.000003		0.86	0.70503	0.00001	−2.7	11.4
Silicocarbonatite (lamprophyric)	MV12·HREE02A	Carb	78.8	10.1	0.07773	0.511573	0.000021	0.510604	8.19	0.70265	0.00003	−2.2	10.6
Silicocarbonatite (lamprophyric)	MV12·HREE02Abis	Carb	41.7	5.0	0.07234	0.511600	0.000005	0.510698	10.04	0.70297	0.00002	−2.2	10.6
Silicocarbonatite (lamprophyric)	MV12·HREE01	BC								0.70352	0.00008	−2.3	11.4
Silicocarbonatite (lamprophyric)	MV12·HREE01	BC	2.8	0.6	0.12793	0.512039	0.000037	0.510444	5.05	0.70294	0.00001		
Silicocarbonatite (kimberlitic)	MV12·KI01	Carb	55.9	11.2	0.12086	0.511584	0.000008	0.510423	−2.13	0.70485	0.00002	−3.9	11.6
Calciocarbonatite	LP12·CACB01A	Carb	1.8	0.3	0.08657	0.511480	0.000021	0.510401	4.20	0.70211	0.00002	−3.2	29.3
Calciocarbonatite	MV12·CACB01Abis	Cal	18.5	4.3	0.13896	0.511831	0.000004	0.510099	−1.71	0.70232	0.00001	−3.4	12.7
Calciocarbonatite	MV12·CACB01B	Cal								0.70197	0.00001	−3.3	8.8
Calciocarbonatite	MV12·CACB01Bbis	Cal								0.70197	0.00001		
Calciocarbonatite	MV13.RAMP2	Carb										−3.8	10.0
Ferrocarbonatite	MV12·CAFECB02	Sid								0.70388	0.00028	−3.7	12.1
Ferrocarbonatite	MV12·CAFECB02	Carb										−3.5	11.3
Ferrocarbonatite	MV12·FECB02	Sid								0.70539	0.00002	−4.1	13.9
Ferrocarbonatite	MV13·FECL1	Carb										−2.2	9.7
Ferrocarbonatite	MV13·FECBAL	Carb										−3.2	11.8
Ferrocarbonatite	MV13FECP	Carb										−2.3	12.0
Ferrocarbonatite (F-alt.)	LP12·UMPO4.A2	Carb	6.4	0.5	0.05108	0.511219	0.000021	0.510582	7.76	0.70205	0.00004	−3.2	10.3
Ferrocarbonatite (F-alt.)	LP12·UMPO4bis	Carb								0.70232	0.00001		
Mixed carbonatites	MV12.LATE1	Cal								0.70193	0.00001	−3.0	9.4
Mixed carbonatites	MV12.LATE2	Sid								0.70229	0.00006	−3.8	9.0
Mixed carbonatites	MV12.LATE2	Carb										−3.4	9.4
Mixed carbonatites	MV12.LATE3.SID	Sid	573	124	0.13104	0.511756	0.000021	0.510123	−1.24	0.70194	0.00001	−3.6	9.9
Mixed carbonatites	MV12.LATE3.CC	Cal	962	213	0.13410	0.512055	0.000021	0.510384	3.86	0.70194	0.00000	−3.4	9.1
Mixed carbonatites	MV13·CACMIX-CC	Carb										−4.6	8.0
Mixed carbonatites	MV13·CACMIX-DOL	Carb										−2.7	9.3
Polygenic breccia	MV12·HREE03	Cal								0.70200	0.00003	−3.6	22.1
Polygenic breccia	MV12.MBX04	Carb	11.6	1.4	0.07384	0.511288	0.000021	0.510368	3.56	0.70201	0.00001	−3.5	35.7
Polygenic breccia	MV12.MBX02B	Carb										−4.0	62.6

The $^{87}Sr/^{86}Sr$ ratios for the Montviel carbonates range from 0.70186 to 0.71190 and are shown in Fig. 8. Carbonates typically have very low Rb concentrations so the measured $^{87}Sr/^{86}Sr$ ratios are assumed to represent initial ratios. Also shown in Fig. 8 are the values for Depleted Mantle (DM), Bulk Earth (BE) and continental crust (CC) reservoirs at 1894 Ma that were calculated using an initial $^{87}Sr/^{86}Sr$ ratio of 0.69898 and a $^{87}Rb/^{86}Sr$ ratio of 0.001, 0.091 and 3, respectively (Allègre 2008). The $^{87}Sr/^{86}Sr$ ratios of the various units range from depleted mantle to more radiogenic crustal values, indicating a mixture of mantle and crustal sources as seen with the Nd isotopes.

The mixing relationship between crustal and mantle reservoirs is less evident from the correlation between ε_{Nd} values and $^{87}Sr/^{86}Sr$ ratios of the granite, lamprophyric and kimberlitic silicocarbonatites, and carbonatites in Fig. 9 compared to the correlation in Fig. 7. This weaker correlation likely results from the difficulty in contaminating the Sr-rich alkaline magmatic fluids with comparatively Sr-poor crustal fluids. At least two carbonate samples from the clinopyroxenite and ijolite are decoupled from this trend. This may reflect overprinting by crustal hydrothermal fluids.

The carbon and oxygen isotope values for the Montviel carbonates are plotted together in Fig. 10. The carbon isotope values range from −5.5 to −2.0‰ VPDB and the oxygen isotope values range from +8.0 to +62.6‰ VSMOW (Fig. 10a). Apart from four samples among the polygenic breccias and carbonatites with heavy $\delta^{18}O$ values between +22.1 and +62.6, most carbonates plot above the carbonatite box (Bell, 1989; Deines, 1989). Samples plotting above the carbonatite box appear to follow a trend of decreasing $\delta^{13}C$ isotope values with increasing $\delta^{18}O$ values such that samples with more crustal $\delta^{18}O$ isotope values have lower, more mantle-like $\delta^{13}C$ isotope values. This trend is also evident in correlations with the Sr isotope compositions of the carbonates in Fig. 11. Carbon and oxygen isotopes correlate well with strontium isotope ratios, but show little to no correlation with neodymium isotopes. The $^{87}Sr/^{86}Sr$ ratios and $\delta^{18}O$ values increase together from $^{87}Sr/^{86}Sr_0$ ratios consistent with the depleted mantle and carbonatite-like $\delta^{18}O$ values of about 9.5 towards higher, more enriched $^{87}Sr/^{86}Sr$ ratios (0.7065) and heavier $\delta^{18}O$ values (13.9). The overall trend is one of progressive contamination of a mantle-derived magma by crustal material that has undergone low temperature alteration. Three samples have $^{87}Sr/^{86}Sr_0$ ratios consistent with the depleted mantle (0.70200 to 0.70210) but have spuriously high ^{18}O values of 22.1 to 35.7 (not shown in Fig. 11a) that likely reflect secondary low temperature hydrothermal alteration.

In contrast, the $\delta^{13}C$ values of the carbonates decrease in two parallel trends towards mantle $\delta^{13}C$ values with increasing $^{87}Sr/^{86}Sr_0$ ratios (Fig. 11c) with the exception of one clinopyroxenite sample (MV12·IJ02) that plots close to the mantle values for both the $^{87}Sr/^{86}Sr_0$ ratios and $\delta^{13}C$ values. The dominant negative trend between the strontium and carbon isotope compositions of the carbonates suggests that increasing crustal contamination of the units was accompanied by depletion in the C isotope composition. The $^{143}Nd/^{144}Nd_0$ vs $\delta^{18}O$ and $^{143}Nd/^{144}Nd_0$ vs $\delta^{13}C$ plots have fewer sample pairs, but the neodymium and oxygen isotopes show a slight trend towards increasing $\delta^{18}O$ values with decreasing $^{143}Nd/^{144}Nd_0$ ratios that is consistent with the strontium and oxygen isotope correlation. There is no real correlation apparent between the neodymium and carbon isotope compositions.

5. Discussion

5.1. Distinct fluid compositions

The objective of this research was to use carbonate minerals as a means to track the evolution of fluids during the petrogenesis of the Montviel alkaline complex and this was possible because the

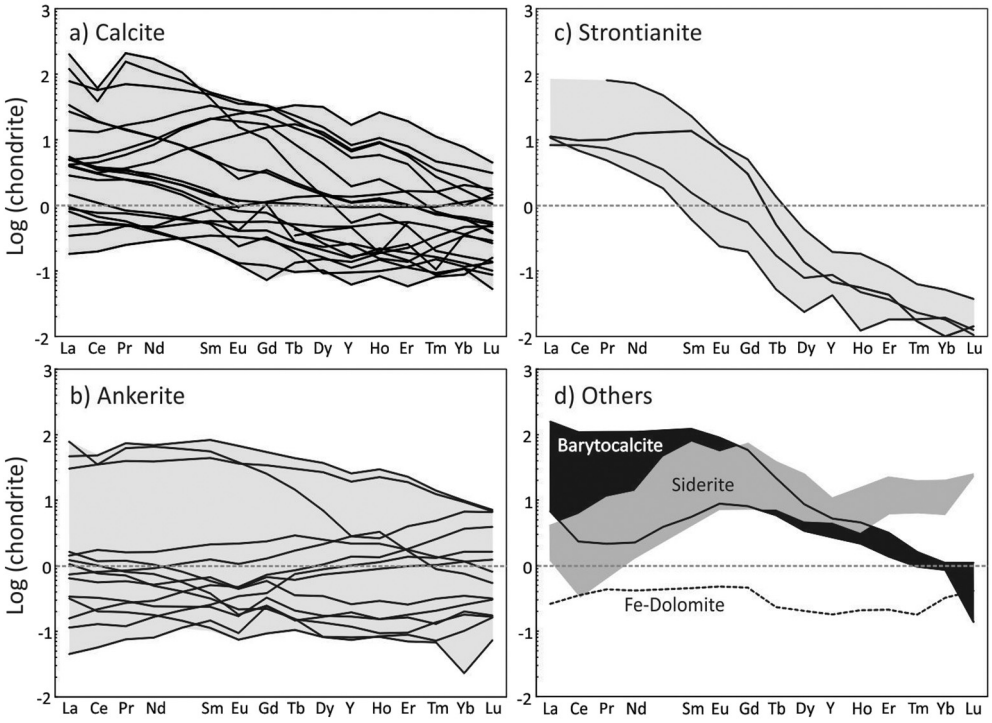

Fig. 4. Chondrite-normalized (McDonough and Sun, 1995) rare earth element concentrations in (a) calcite, (b) ankerite, (c) strontianite, and (d) barytocalcite, strontianite and ferroan-dolomite, from all lithologies at Montviel. 1σ standard deviations are reported in Table 1.

geochemical and isotopic compositions of Montviel's carbonates reflect their magmatic, metasomatic (alteration) or hydrothermal (infills) origin. Previous work at Montviel has demonstrated that rocks were strongly metasomatized and that their geochemical and isotopic signatures were reflective of the metasomatic fluids (Nadeau et al. 2015, 2016a, 2016b). Metasomatic biotite and aegirine-augite from clinopyroxenite, melteigite, ijolite, melanosyenite and granite show trace element signatures that are systematically different than those from silicocarbonatites, calciocarbonatites, ferrocarbonatites and polygenic breccia, suggesting that the metasomatic event overprinting the silicate rocks was distinct from that overprinting the carbonatites, and demonstrating that each injection of magma was accompanied by its own fluids (Nadeau et al., 2016a). The ε_{Nd} of metasomatic biotite, aegirine-augite and of whole rocks was interpreted to show that each of these fluids were actually mixtures of mantle and crustal fluids (Nadeau et al., 2016a).

We argue that the metasomatic and hydrothermal carbonates present in the silicate rocks and in the carbonatites were produced by two different fluids that accompanied these two different magmas. This argument is based on the different chondrite-normalized REE patterns (Fig. 5) and MORB-normalized LILE-HFSE spidergrams (Fig. 6) for carbonates from the different lithologies present at Montviel. Because the four volatile-saturated magma injections originated from the same depleted-mantle source and because their fluids mixed with the same (or similar) crustal fluids, the isotopes still show simple binary mixing between two sources. In contrast, the carbonates precipitating from these four distinct fluids do show distinct trace element signatures.

The first fluid that was injected with clinopyroxenite was enriched in REE, and especially in LREE, as carbonates from clinopyroxenite have negative slopes of 100 times chondrites for LREE to 1 times chondrites for HREE (Fig. 5a). The REE were subsequently depleted in fluids from co-magmatic syenites, melteigites and ijolites as well as in granites. This could have resulted from the extraction of carbonatite out from the source of clinopyroxenite and partitioning of the REE with the carbonatite, but could also have resulted from dilution of the REE-rich mantle fluids by REE-depleted crustal fluids. These lithologies were then cut by: (1) lamprophyric silicocarbonatite accompanied by fluids from the depleted mantle (Figs. 7–9) hosting moderate concentrations of LREE (Fig. 5e); and (2) calciocarbonatite with fluids having limited REE concentrations but negative to flat and positive slopes (Fig. 5f), suggesting that a mechanism was operating which was preferentially enriching the MREE to HREE elsewhere in the alkaline complex. Evidence for this this mechanism is found in coexisting LREE-enriched and HREE-enriched ferrocarbonatites (Fig. 5g-h), where carbonates show negative to positive REE profiles (LREE-rich ferrocarbonatites) to concave down REE profiles (HREE-rich ferrocarbonatites). The mixed carbonatites that followed probably had fluids evolving in a similar manner but limited data precludes much discussion about their evolution, apart from the fact that they were also accompanied by MREE to HREE (Fig. 5i).

The evolution of the LILE (Sr, Ba) and HFSE (Th, Ta, Nb, Zr, Hf, Ti) can be compared with that of REE by observing the incompatible element spidergrams (Fig. 6). The decrease in REE concentrations in fluids from clinopyroxenites, melteigites and ijolites is accompanied by an increase in group 4 (Ti-Zr-Hf) and group 5 (Nb—Ta) transition metals (Fig. 6a-d). Similarly, in silicocarbonatite and calciocarbonatite, the low REE concentrations are coupled to variably enriched Ti-Zr-Hf and Nb—Ta concentrations (Fig. 6e-f). In LREE-bearing ferrocarbonatites, the high REE concentrations are again paired with very low concentrations of the group 4–5 transition metals whereas in HREE-bearing ferrocarbonatites, the high REE concentrations are sometimes coupled with high concentrations of group 4–5 transition metals (Fig. 6g-h). Similarly in the mixed carbonatites and the polygenic breccias, carbonates which were enriched in HREE show enrichment in Ti-Zr-Hf-Nb-Ta (Fig. 6i-j). This suggests that the mechanism by which the LREE are enriched into the fluid phase also depletes the fluid in group 4–5 transition metals, but that the process through which the HREE are enriched, i.e. in HREE-ferrocarbonatites, mixed carbonatites and polygenic

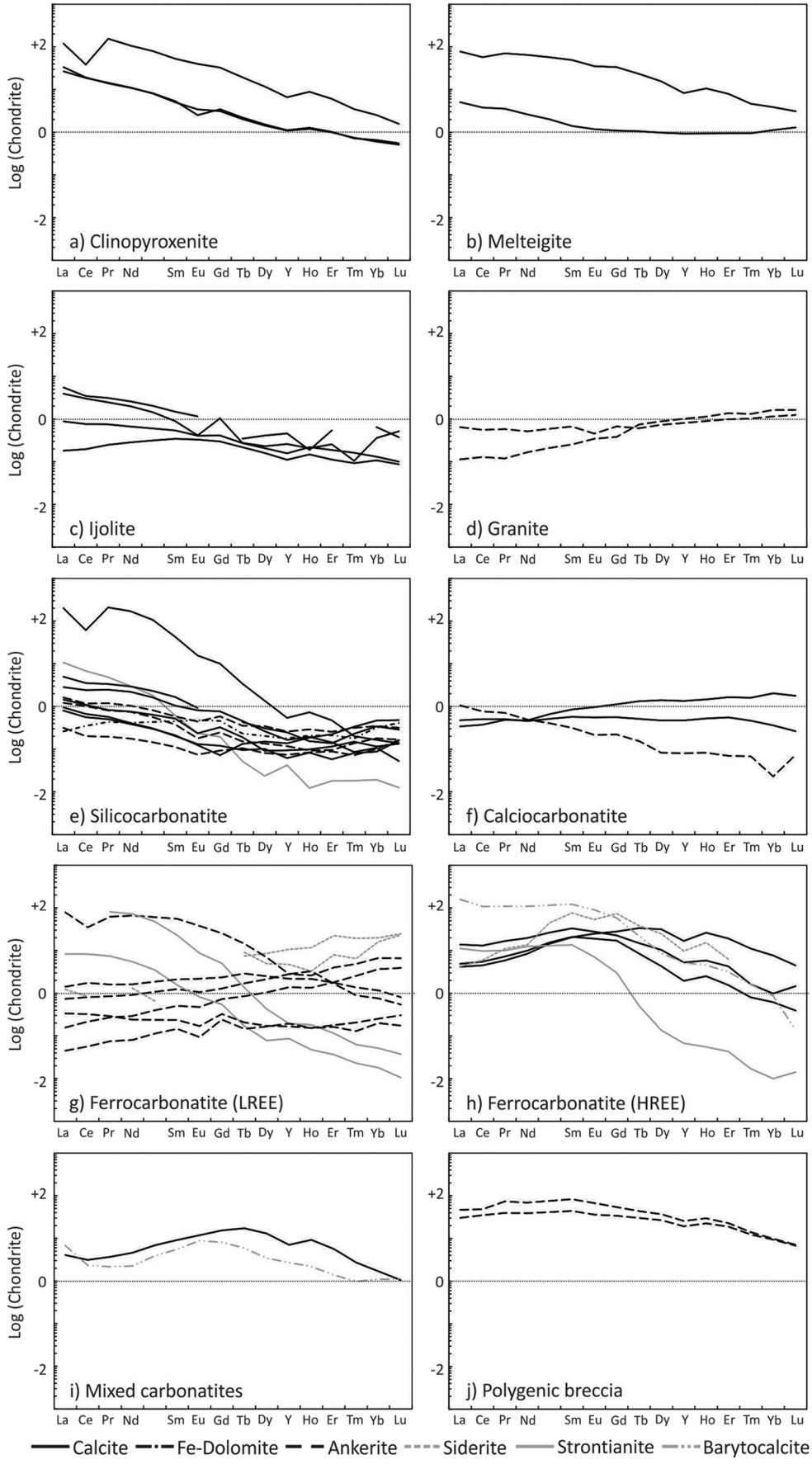

Fig. 5. Chondrite-normalized (McDonough and Sun, 1995) rare earth element concentrations in carbonates from the different lithologies at Montviel. 1σ standard deviations are reported in Table 1.

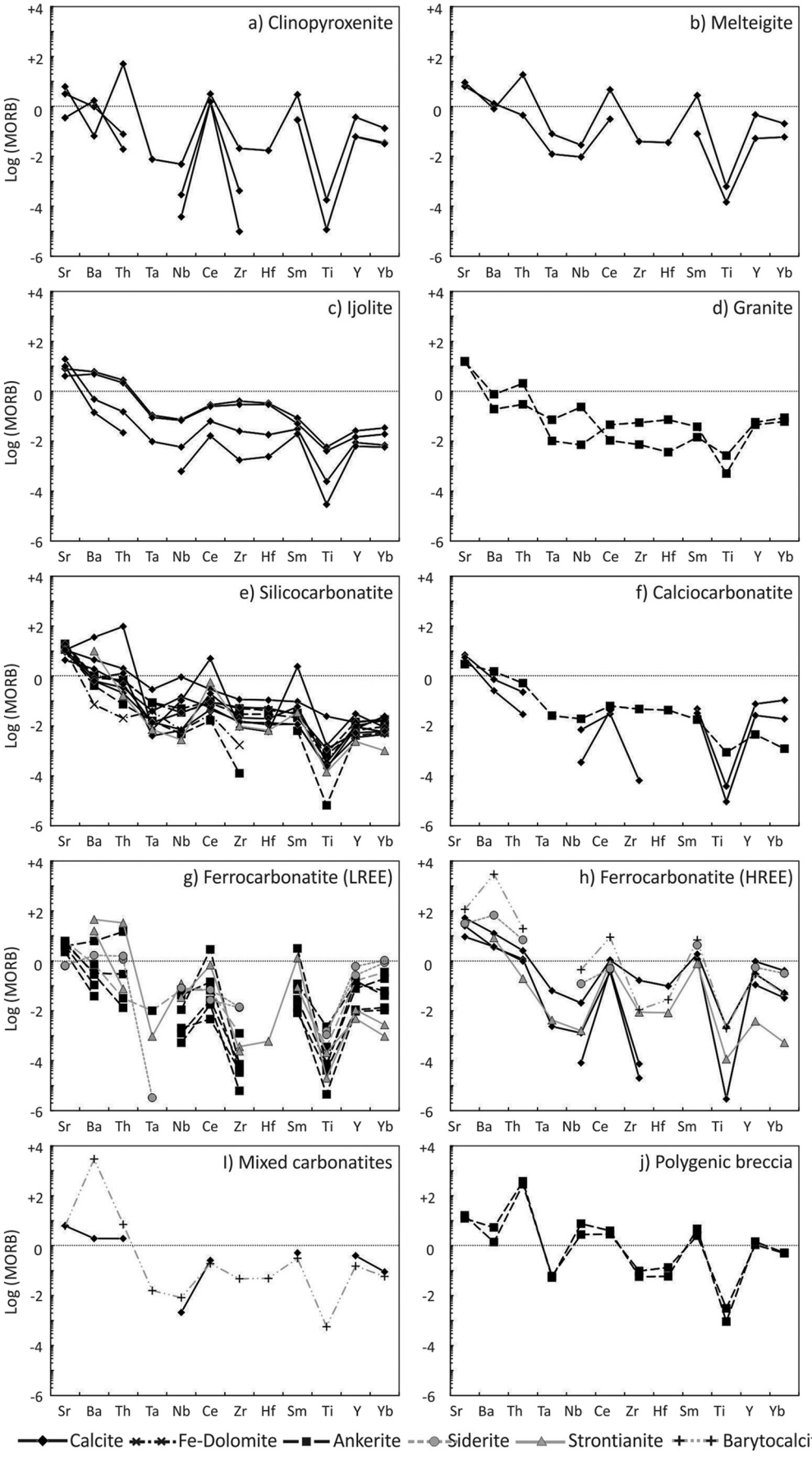

Fig. 6. MORB-normalized (McDonough and Sun, 1995) incompatible element concentrations in carbonates from the different lithologies at Montviel. 1σ standard deviations are reported in Table 1.

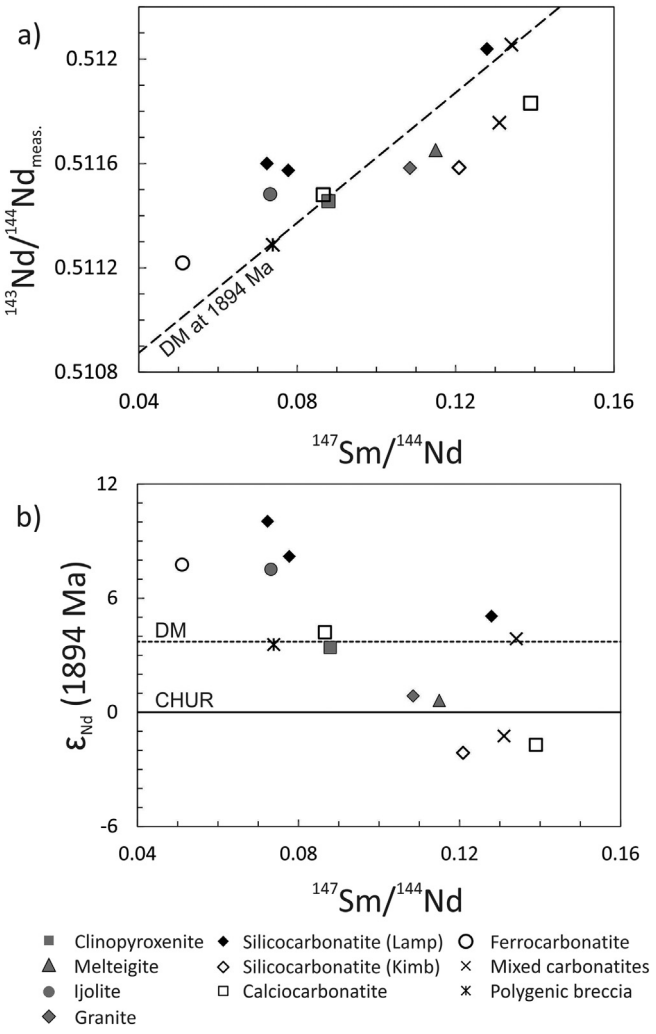

Fig. 7. $^{143}Nd/^{144}Nd_{measured}$ vs $^{147}Sm/^{144}Nd$ (a) and ε_{Nd} vs $^{147}Sm/^{144}Nd$ (b) for carbonates from the different lithologies at Montviel (See Table 2). The depleted mantle (DM) isochron was arbitrarily fitted using the U–Pb zircon 1894 Ma age of the alkaline complex (David et al., 2006) with a depleted mantle $^{143}Nd/^{144}Nd_{initial}$ of 0.510376. 2σ errors are reported in Table 2 and are smaller than the symbols. The initial ε_{Nd} value of the chondritic uniform reservoir (CHUR) was calculated based on an present day $^{143}Nd/^{144}Nd$ ratio of 0.512638 and $^{147}Sm/^{144}Nd$ ratios of 0.1966 (Allègre, 2008). The depleted mantle (DM) ε_{Nd} was calculated following Bennett and DePaolo (1987).

breccia, does not further deplete, and possibly even enriches the group 4–5 HFSE in the fluid. The simplest way to explain the different behavior of REE and group 4–5 HFSE is through their different mobility and their different affinity for acidity. The ionic potential (charge/radius) of REE is lower than that of group 4–5 HFSE, making REE generally more mobile in volatile phases. This behavior is present at Montviel where the REE are affected by hydrothermal processes and where Ti-Zr-Hf-Ta do not show anomalously high concentrations. Indeed, most hydrothermal Zr-Hf-Nb-Ta deposits are associated with acidic fluid-bearing silicate magmas (Wood, 2005) and are not related with carbonatites magmas (e.g., Salvi and Williams-Jones, 1996; Linnen and Cuney, 2005; Sheard et al., 2012). The gradual unmixing of volatile-saturated carbonatite- and silicate magmas would produce two fluid phases. The fluid phase associated with the carbonatite magmas would be increasingly enriched in REE and depleted in group 4–5 HFSE while fluids associated with the silicate magma would be depleted in REE and enriched in group 4–5 HFSE. Pulses of REE-rich, Ti-Zr-Hf-Nb-Ta-poor, neutral-to-alkaline fluids would thus result from unmixing events between carbonatite and silicate magmas in the mantle. In other words, immiscibility and unmixing of silicate and carbonatite magma and their coexistence with volatile phases may be at the origin of the REE-bearing carbonatites at Montviel.

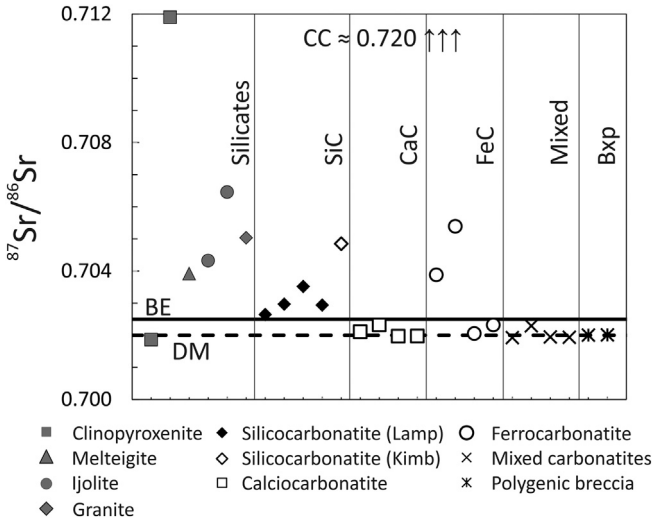

Fig. 8. $^{87}Sr/^{86}Sr$ ratios for carbonates from the different lithologies from Montviel (See Table 2). 2σ error are small than the symbols and are reported in Table 2. The $^{87}Sr/^{86}Sr$ ratios for depleted mantle (DM; 0.701954), bulk earth (BE; 0.70249) and continental crust (CC; 0.720) at 1894 Ma were calculated based on a basaltic achondrite best initial (BABI) of 0.698980 and $^{87}Rb/^{86}Sr$ ratios of 0.001, 0.0847 and 0.3, respectively (Faure, 1977; Allègre, 2008).

5.2. Decoupling of Sr-C-O and Nd isotopes

The correlations between the Sr, C and O isotope compositions in carbonates from Montviel (Fig. 11a,c) suggests that Sr, C and O can be used to track the sources of the fluids and to provide information about the geological processes involving these fluids. The same cannot be said for the Nd isotope compositions due to the weaker correlation between this system and the other isotopic systems (Fig. 9, 11b,d). However, both the Nd and Sr isotopes illustrate that mixing of crustal and mantle magmas/fluids were instrumental in the evolution of the Montviel system. Both the Nd and $^{87}Sr/^{86}Sr$ ratios vary systematically in carbonates from each of the lithologies of the alkaline complex from depleted mantle values of about 0.702 ($^{87}Sr/^{86}Sr$) and +10 (ε_{Nd}) to gradually more radiogenic Sr (0.706 to 0.712) and less radiogenic

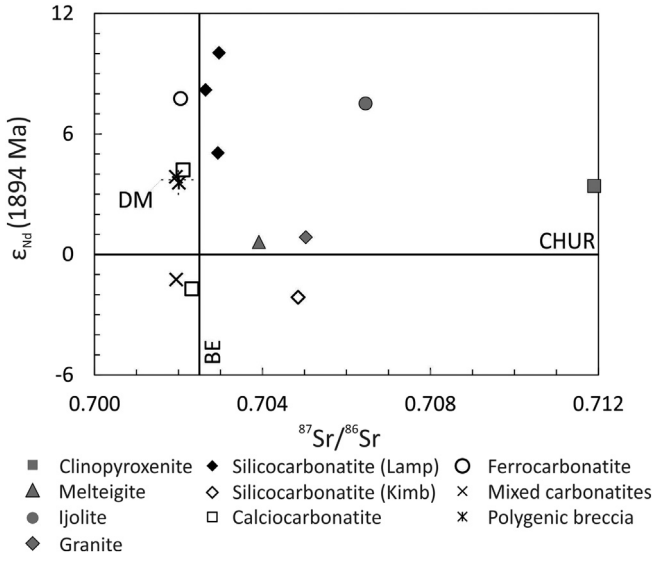

Fig. 9. Coupled ε_{Nd} and $^{87}Sr/^{86}Sr$ data for carbonates from Montviel. Carbonates do not have significant amounts of Rb so the ratios are assumed to be equivalent to initial values. 2σ errors are reported in Table 2 and are smaller than the symbols. DM depleted mantle; BE bulk Earth; CHUR chondritic uniform reservoir.

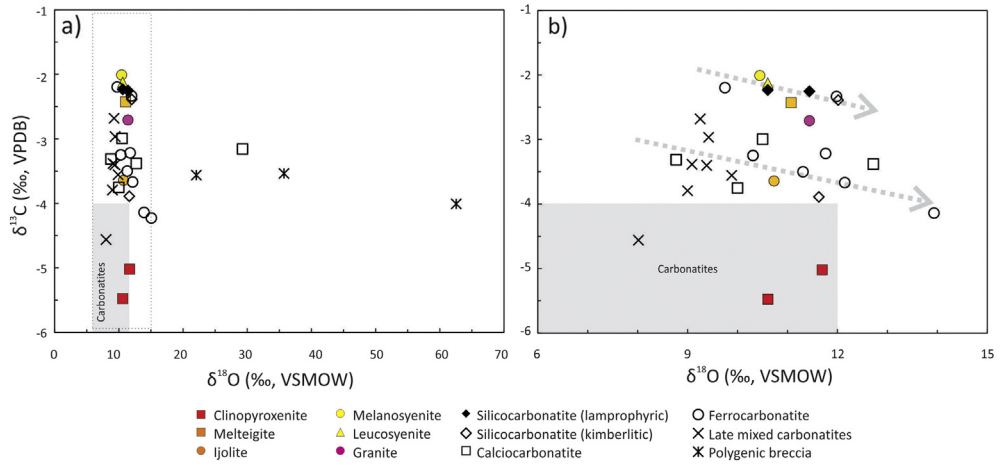

Fig. 10. $\delta^{13}C$ vs $\delta^{18}O$ data for carbonates from Montviel. 2σ relative standard errors are 0.07‰ and 0.19‰ for $\delta^{13}C$ and $\delta^{18}O$ values, respectively. The carbonatite box is from Bell (1989) and the marine carbonates box is from Kerrich et al., 1987. The inset box in (a) is shown in (b).

ε_{Nd} (−4) isotope compositions that are consistent with crustal contamination. As noted above, the carbon and oxygen isotopic ratios also vary in a systematic manner, extending from the carbonatite box (Bell, 1989; Deines, 1989) to heavier C and O isotopic ratios of −2.0 and +13.9, respectively, apart from the four anomalous $\delta^{18}O$ values between +22.1 and +62.6 that probably represent low temperature, secondary carbonates. The $\delta^{18}O$ values of the carbonates correlate well with $^{87}Sr/^{86}Sr$ ratios, varying from about +9 to +13‰ as Sr isotope ratios vary from depleted mantle to crustal values. The trend of lighter $\delta^{13}C$ values with increasing $\delta^{18}O$ values and $^{87}Sr/^{86}Sr$ ratios of the carbonates (Figs. 9b, 10c) suggests that crustal fluids contained reduced carbon. A similar negative correlation between carbon and oxygen isotopes was observed among carbonate clasts in the Timiskaming sediments of Abitibi (Legault and Hattori, 1994) and may reflect incorporation of reduced carbon from metamorphic and sedimentary units within the Abitibi crust (e.g. Kerrich et al., 1987).

Hence it is likely that the fluids from which the carbonates precipitated evolved from heavy to light C isotope ratios, light to heavy O isotope ratios, and depleted to radiogenic Sr isotope ratios by mixing with fluids derived from crustal sources, along the trends illustrated

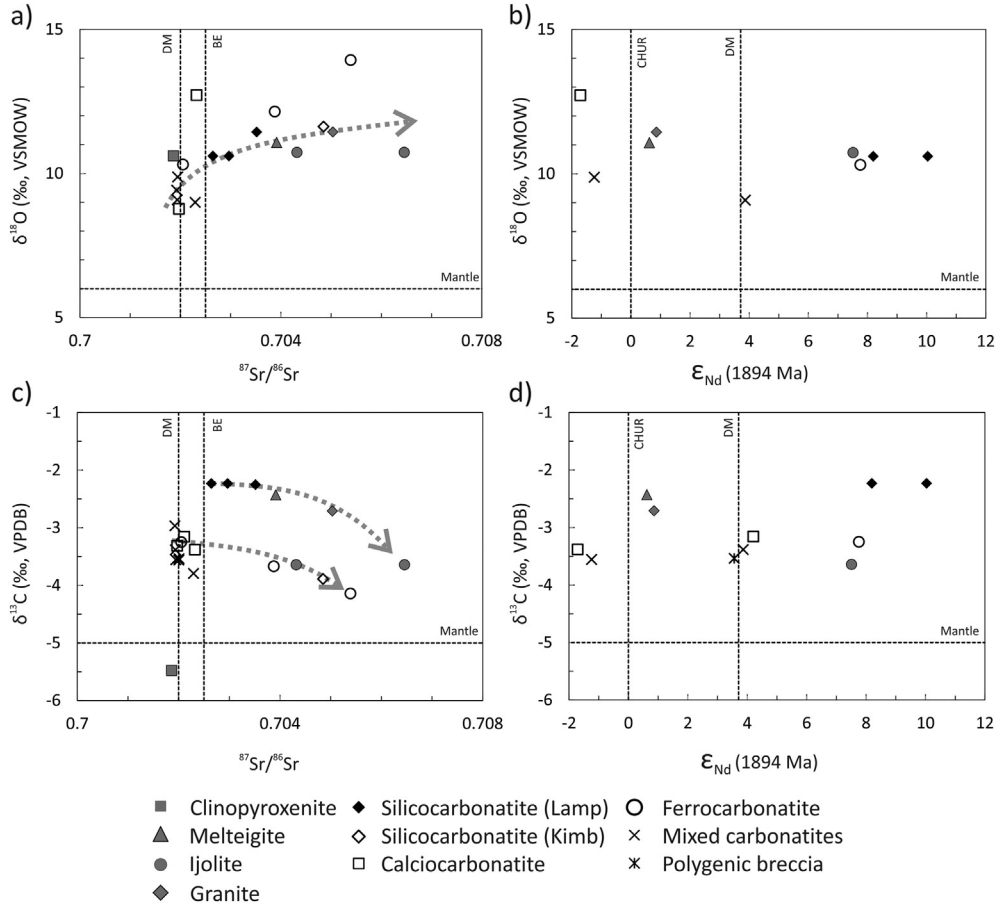

Fig. 11. $\delta^{18}O$ vs $^{87}Sr/^{86}Sr$ (a), $\delta^{18}O$ vs ε_{Nd} (b), $\delta^{13}C$ vs $^{87}Sr/^{86}Sr$ (c) and $\delta^{13}C$ vs ε_{Nd} (d) for carbonates from Montviel. The $\delta^{13}C$ and $\delta^{18}O$ mantle values are from Bell (1989). 2σ relative standard errors are 0.07‰ and 0.19‰ for $\delta^{13}C$ and $\delta^{18}O$ values, respectively, and are smaller than the symbols and reported in Table 2 for $^{143}Nd/^{144}Nd$ and $^{87}Sr/^{86}Sr$ values.

by dashed gray arrows in Figs. 10b, 11a,c. This is in contrast to many other carbonatites which evolve towards heavier C and O isotope ratios on $\delta^{13}C$ vs $\delta^{18}O$ plots. This evolution towards heavier isotope ratios is interpreted to be the product of fractional crystallization during cooling (e.g., Ray and Ramesh, 2000) and/or increasing fluid-rock ratios (Boulvais et al., 1998; Nadeau et al., 2014). None of the Montviel C and O isotope data plot at mantle values. This may reflect C-isotope fractionation between the carbonatite magma, the fluid, and the carbonate minerals that occurred during cooling, which implies that the analyzed carbonates are hydrothermal (or carbothermal) carbonates rather than magmatic.

Four of the carbonate samples representing three different units yield ε_{Nd} values (+7.5 to +10) that are more depleted than the modeled depleted mantle at 1894 Ma (e.g. +3.7; DePaolo 1981). Such ultra-depleted compositions are rare, but have also been reported for 1.8 Ga mafic volcanic rocks in Antarctica (+8.2; Sivell and McCulloch, 1991) and 1.7 Ga granitoids from the southwestern United States (+7.7; Condie et al., 1999). Alternatively, the high ε_{Nd} values may reflect perturbation of the Sm—Nd system due to the mobility of the REE in the Montviel system. Mantle fluids may have remobilized the REE and redistributed Sm/Nd ratios as well as whole REE profiles at the magmatic reservoir scale, which subsequently acted as mantle source for the alkaline carbonatite magmas and fluids and the actual carbonatite-hosted REE-Nb deposit. The fluids which redistributed the REE in carbonatites must have been neutral to alkaline for carbonates to be stable, and must have transported the REE via hydrated carbonic complexes (Williams-Jones et al., 2012). In contrast, fluids which accompanied the silicate magmas must have been neutral to slightly acidic (Webster and Mandeville, 2007) and must have transported the REE by complexation with chloride (Williams-Jones et al., 2012). Although carbonates had concentrations of REE similar in clinopyroxenite, silicocarbonatite and carbonatites, the REE-bearing carbonates and fluorocarbonates such as burbankite-(Ce), cordylite-(Ce), huanghoite-(Nd) and ewaldite-(Y) had REE averaging around 16.4 ± 10.7 wt% total REE, and were found almost only in silicocarbonatites and carbonatites, suggesting that the REE partitioned preferentially into the CO_3^{2-}-bearing, alkaline pH fluid, over the silicate-bearing, acidic fluid. The gradual exsolution of carbonatite magma out of a silicate source (a metasomatized mantle or a melt?) interpreted from the spidergrams in Fig. 6 is consistent with the petrogenesis of carbonatites (e.g., Bell, 1998; Harmer and Gittins, 1998; Lee and Wyllie, 1998) and would also have made fluids which were gradually more enriched in transporting ligands such as Cl in the silicate-bearing fluid and CO_3^{2-} in the carbonate-bearing fluid.

6. Conclusions

The analysis of major, minor and trace elements as well as $\delta^{18}O$, $\delta^{13}C$, $^{87}Sr/^{86}Sr$ and $^{143}Nd/^{144}Nd$ in what are mostly hydrothermal and metasomatic carbonates from Montviel alkaline complex and associated carbonatite-hosted hydrothermal REE deposit show that each of the four injections of mantle magmas were accompanied by a volatile phase, and that the hydrothermal/metasomatic carbonates now present in these rocks are representative of the magmas in which they precipitated. In this respect, carbonates from clinopyroxenite precipitated from fluids akin to clinopyroxenite parent magma, and carbonates from carbonatite precipitated from fluids accompanying carbonatite magma. The variations in REE, LILE and HFSE in carbonates from these lithologies suggest that carbonatite melt might have been exsolving out from a silicate-rich source such as a pre-metasomatized (carbonated) mantle or hybrid silicate carbonatite magma, and that the fluid composition evolved towards higher REE and lower HFSE with increasing degree of segregation of the carbonatite magma and its silicate source. The C-O-Sr isotopic systems were well correlated among themselves and show that a depleted mantle fluid gradually mixed with crustal fluids, leading to increasingly radiogenic Sr isotope ratios and driving the C and O isotopic ratios towards respectively lighter and heavier values. The Sm—Nd system does not correlate as strongly as the C-O-Sr isotopic systems but the Sm/Nd isotopic system does preserve evidence of the interaction between depleted mantle and crustal magmas and fluids at Montviel.

Acknowledgements

This research benefited from NSERC grants to RS and MJ and from a FRQNT post-doctoral scholarship to ON. We would like to acknowledge the technical, logistical, scientific and financial contribution of Ressources Géoméga Inc. We also thank L. Shi for help with EMPA analyses, A. Poirier for help with the radiogenic isotopes, and JF. Hélie for the C and O isotope analyses.

References

Allègre, C.J., 2008. Isotope Geology. Cambridge University Press, Edinburg, UK.
Barker, A.L., 1975. Summary report on exploration work. Rapport statutaire déposé au ministère des Ressources Naturelles et de la Faune, Québec, p. 133 GM 31071.
Bell, K., 1989. Carbonatites, Genesis and Evolution, GAC-MAC 1986. Unwin Hyman Ltd., London, Ottawa-Carleton Geoscience Centre 618 pages.
Bell, K., 1998. Radiogenic isotope constraints on relationships between carbonatites and associated silicate rocks; a brief review. Journal of Petrology 39, 1987–1996.
Bell, K., Blenkinsop, J., Kwon, S.T., Tilton, G.R., Sage, R.P., 1987. Age and radiogenic isotopic systematics of the Borden carbonatite complex, Ontario, Canada. Canadian Journal of Earth Sciences 24, 24–30.
Bennett, V.C., DePaolo, D.J., 1987. Proterozoic crustal history of the western United States as determined by neodymium isotopic mapping. Geological Society of America Bulletin 99, 674–685.
Boulvais, P., Fourcade, S., Gruau, G., Moine, B., Cuney, M., 1998. Persistence of pre-metamorphic C and O isotopic signatures in marbles subject to pan-African granulite-facies metamorphism and U–Th mineralization (Tranomaro, Southeast Madagascar). Chemical Geology 150, 247–262.
Chiarabba, C., Giacomuzzi, G., Bianchi, I., Agostinetti, N.P., Park, J., 2014. From underplating to delamination-retreat in the northern Apennines. Earth and Planetary Science Letters 403, 108–116.
Condie, K., Latysh, N., Van Schmus, W.R., Kozuch, M., Selverstone, J., 1999. Geochemistry, Nd and Sr isotopes, and U-Pb zircon ages of granitoid and metasedimentary xenoliths from the Navajo volcanic field, four corners area, southwestern United States. Chemical Geology 156, 95–133.
Condie, K., Pisarevsky, S.A., Korenaga, J., Gardoll, S., 2015. Is the rate of supercontinent assembly changing with time? Precambrian Research 259, 278–289.
Corta, H., Berthelot, P., 2002. Rapport d'une campagne de sondages. Propriété Montviel. Resources Nomans Inc., MRNF GM59647, Québec, Canada.
David, J., Dion, C., Goutier, J., Roy, P., Bandyayera, D., Legault, M., Rhéaume, P., 2006. Datations U-Pb effectuées dans la Sous-province de l'Abitibi à la suite des travaux de 2004–2005. RP2006-04 22 pages.
Deines, P., 1989. Stable isotope variations in carbonatites. In: Bell, K. (Ed.), Carbonatites; Genesis and Evolution. Unwin Hyman, London, United Kingdom, pp. 301–359.
DePaolo, D.J., 1981. Trace element and isotopic effects of combined wallrock assimilation and fractional crystallization. Earth and Planetary Science Letters 53, 189–202.
Desharnais, G., Duplessis, C., 2011. Montviel Core Zone REE Mineral Resource Estimate Technical Report, Quebec, 43101-Compliant Professional Report 74 pages.
Faure, G., 1977. Principles of Isotope Geology. John Wiley and Sons, USA.
Goutier, J., 2006. Géologie de la région du lac au Goéland (32F15), RG 2005-05 39 pages.
Harmer, R.E., Gittins, J., 1998. The case of primary, mantle-derived carbonatite magma. Journal of Petrology 39, 1895–1903.
Hecht, L., Freiberger, R., Gilg, H.A., Grundmann, G., Kostitsyn, Y.A., 1999. Rare earth element and isotope (C, O, Sr) characteristics of hydrothermal carbonates: genetic implications for dolomite-hosted talc mineralization at Göpfersgrün (Fichtelgebirge, Germany). Chemical Geology 155, 115–130.
Jebrak, M., 1997. Hydrothermal breccias in vein-type ore deposits; a review of mechanisms, morphology and size distribution. Ore Geology Reviews 12, 111–134.
Kerrich, R., Fryer, B.J., King, R.W., Willmore, L.M., Van-Hees, E., 1987. Crustal outgassing and LILE enrichment in major lithosphere structures, Archean Abitibi greenstone belt; evidence on the source reservoir from strontium and carbon isotope tracers. Contributions to Mineralogy and Petrology 97, 156–168.
Le Bas, M.J., 1987. Nephelinites and carbonatites. Geological Society Special Publication 30, 53–83.
Lee, W.-J., Wyllie, P.J., 1998. Processes of crustal carbonatite formation by liquid immiscibility and differentiation, elucidated by model systems. Journal of Petrology 39, 2005–2013.
Legault, M.I., Hattori, K., 1994. Provenance of igneous clasts in conglomerates of the Archaean Timiskaming group, Kirkland Lake area, Abitibi greenstone belt, Canada. Canadian Journal of Earth Sciences 31, 1749–1762.
Linnen, R.L., Cuney, M., 2005. Granite-related rare-element deposits and experimental constraints on Ta-Nb-W-Sn-Zr-Hf mineralization. Short Course Notes - Geological Association of Canada 17, 45–68.
McDonough, W.F., Sun, S.S., 1995. The composition of the earth. Chemical Geology 120, 223–253.

Mulja, T., 2006. The Mineralogy of Samples from a Rare-Earth Element Prospect and a Base-Metal Prospect for Niogold Mining Corporation. Niogold, MRNF GM62438. Canada, Québec.
Nadeau, O., Cayer, Al., Pelletier, M., Séguin, D., Stevenson, R., Jébrak, M., 2013. Pétro-métallogenèse du système alcalin carbonatitique (REE-Nb) de Montviel, Abitibi. Ministère des Ressources Naturelles et de la Faune, Q.Québec Mines, Canada
Nadeau, O., Stevenson, R., Jébrak, M., 2014. The Archean magmatic-hydrothermal system of Lac Shortt (Au, REE), Abitibi, Canada: insights from carbonate fingerprinting. Chemical Geology 387, 144–156.
Nadeau, O., Cayer, A., Pelletier, M., Stevenson, R., Jébrak, M., 2015. The Paleoproterozoic Montviel carbonatite-hosted REE–Nb deposit, Abitibi, Canada: geology, mineralogy, geochemistry and genesis. Ore Geology Reviews 67, 314–335.
Nadeau, O., Stevenson, R., Jébrak, M., 2016a. Evolution of Montviel alkaline-carbonatite complex by coupled fractional crystallization, fluid mixing and metasomatism – part I: petrography and geochemistry of metasomatic aegirine-augite and biotite: implications for REE-Nb mineralization. Ore Geology Reviews 1143–1162.
Nadeau, O., Stevenson, R., Jébrak, M., 2016b. Evolution of Montviel alkaline-carbonatite complex by coupled fractional crystallization, fluid mixing and metasomatism – part II: trace element and Sm-Nd isotope geochemistry of metasomatic rocks: implications for REE-Nb mineralization. Ore Geology Reviews 72, 1163–1173.
Pirajno, F., 2013. Effects of Metasomatism on Mineral Systems and their Host Rocks; Alkali Metasomatism, Skarns, Greisens, Tourmalinites, Rodingites, Black-Wall Alteration and Listvenites. In: Harlov, D.E., Austrheim, H. (Eds.), Metasomatism and the Chemical Transformation of Rock; the Role of Fluids in Terrestrial and Extraterrestrial Processes. Springer, Berlin, Germany, pp. 203–251.
Ray, J.S., Ramesh, R., 2000. Rayleigh fractionation of stable isotopes from a multicomponent source. Geochimica et Cosmochimica Acta 64, 299–306.
Roulleau, E., Stevenson, R., 2013. Geochemical and isotopic (Nd–Sr–Hf–Pb) evidence for a lithospheric mantle source in the formation of the alkaline Monteregian Province (Quebec). Canadian Journal of Earth Sciences 50, 650–666.
Sage, R.P., 1988. Geology of Carbonatite-Alkalic Rock Complexes in Ontario; Cargill Township Carbonatite Complex, District of Cochrane. Ontario Geological Survey, Ontario, Canada 92 pages.
Salvi, S., Williams-Jones, A.E., 1996. The role of hydrothermal processes in concentrating high-field strength elements in the Strange Lake peralkaline complex, northeastern Canada. Geochimica et Cosmochimica Acta 60, 1917–1932.
Sheard, E.R., Williams-Jones, A.E., Heiligmann, M., Pederson, C., Trueman, D.L., 2012. Controls on the concentration of zirconium, niobium, and the rare earth elements in the Thor Lake rare metal deposit, northwest territories, Canada. Economic Geology 107, 81–104.
Sivell, W.J., McCulloch, M.T., 1991. Neodymium isotope evidence for ultra-depleted mantle in the early Proterozoic. Nature 354, 384–387.
Smithies, R.H., Champion, D.C., 1999. Late Archaean felsic alkaline igneous rocks in the eastern goldfields, Yilgarn craton, Western Australia; a result of lower crustal delamination? Journal of the Geological Society of London 156, 561–576 Part 3.
Webster, J.D., Mandeville, C.W., 2007. Fluid immiscibility in volcanic environments. Reviews in Mineralogy and Geochemistry 65, 313–362.
Williams-Jones, A.E., Migdisov, A.A., Samson, I.M., 2012. Hydrothermal mobilisation of the rare earth elements; a tale of 'ceria' and 'yttria. Elements 8, 355–360.
Wood, S.A., 2005. The aqueous geochemistry of zirconium, hafnium, niobium and tantalum. Short Course Notes - Geological Association of Canada 17, 217–268.